minerals

MDPI

Article

Pyrite Textures, Trace Element Geochemistry and Galena Pb Isotopes of the Yanzhupo Gold Deposit in the Jiangnan Orogen, South China: Implications for Gold Mineralization Genesis

Jia Liao [1,2,3], Xu Wang [2,3,*], Biao Chen [1], Buqing Wang [1], Zhenhua Zhu [1], Wentao Wang [1], Ding Peng [1], Qian Zhang [1], Zhuang Liu [1] and Qiangqiang Xu [1]

[1] Changsha General Survey of Natural Resources Center, China Geological Survey, Changsha 410600, China; liaojia2143@163.com (J.L.); cbiao1211@sina.com (B.C.); wbq555@zuaa.zju.edu.cn (B.W.); 15628596220@163.com (Z.Z.); 18570603001@163.com (W.W.); 18570921623@163.com (D.P.); zq18419756828@163.com (Q.Z.); zhuang_yy2011@163.com (Z.L.); xuqiangqiang2025@163.com (Q.X.)
[2] Key Laboratory of Metallogenic Prediction of Nonferrous Metals and Geological Environment Monitoring, Central South University, Ministry of Education, Changsha 410083, China
[3] School of Geosciences and Info-Physics, Central South University, Changsha 410083, China
* Correspondence: 245003004@csu.edu.cn

Abstract: The northeastern Hunan district in the Jiangnan Orogen (South China) holds significant gold resources, whose genesis remains perplexing, especially in terms of the gold source and mineralization process. Yanzhupo (2.50 t @ 2.52 g/t) is a newly discovered gold deposit in the northeastern Hunan district and is characterized by multiple generations of pyrite. Its alteration/mineralization can be divided into three stages: (I) quartz-ankerite-pyrite; (II) quartz-ankerite-chlorite-pyrite-gold; (III) quartz-ankerite-calcite-pyrite. Petrographic observations and back-scattered electron (BSE) imaging revealed six generations of pyrite: Cu-Au rich bright rims (Py1a) and porous cores (Py1b) in Stage I, Py2a with homogenous textures, Py2b with oscillatory zoning and Py2c with homogenous textures in Stage II and Py3 with homogenous textures in Stage III. Galena Pb isotopes, similar to the Wangu deposit, and pyrite chemical compositions show that the ore-forming materials of Yanzhupo came from deep magma, and some metal elements may be extracted from deep basement by fluid-mineral interactions during the upward migration of hydrothermal-magmatic fluid. The positive correlation between Cu and Au in pyrite reflects the oxidized ore-forming fluids. The enrichment of Cu and Au in Py1a reflects the precipitation of pyrite under high temperature fluid, forming the primary enrichment of Au. Porous Py1b is characterized by lower trace elements than Py1a, sharp reaction front and rich chalcopyrite and galena inclusions, indicating Py1b formed via coupled dissolution-reprecipitation (CDR) reactions of Py1a. The CDR reactions promoted by the oxidizing fluid itself re-release Au into the fluid. From Py2a to Py2c, the contents of As, Sb and Pb first increased and then decreased, which may reflect the increase of fluid pH caused by sulfidation of the wall rocks and the impoverishment of ore-forming fluids caused by the precipitation of a large number of elements. The sulfidation of the wall rocks in Stage II destroyed the stability of the $Au(HS)_2^-$ and Au $(HS)S_3^-$ complexes and led to the deposition of native gold. The barren ore-forming fluids precipitated homogenous Py3 in a stable environment. Therefore, we think that the Yanzhupo gold deposit may have been associated with magmatic-hydrothermal activity, and the mineralization mechanism may be CDR reactions and sulfidation of the wall rocks.

Keywords: pyrite trace elements; galena Pb isotopes; mineralization mechanism; Yanzhupo gold deposit; Jiangnan Orogen

Academic Editor: Galina Palyanova

Received: 3 December 2024
Revised: 14 January 2025
Accepted: 15 January 2025
Published: 20 January 2025

Citation: Liao, J.; Wang, X.; Chen, B.; Wang, B.; Zhu, Z.; Wang, W.; Peng, D.; Zhang, Q.; Liu, Z.; Xu, Q. Pyrite Textures, Trace Element Geochemistry and Galena Pb Isotopes of the Yanzhupo Gold Deposit in the Jiangnan Orogen, South China: Implications for Gold Mineralization Genesis. *Minerals* **2025**, *15*, 94. https://doi.org/10.3390/min15010094

Correction Statement: This article has been republished with a minor change. The change does not affect the scientific content of the article and further details are available within the backmatter of the website version of this article.

1. Introduction

Pyrite is one of the most common sulfides on Earth and an important Au-bearing ore mineral in various types of gold deposits [1–4]. Previous studies have shown that pyrite is often enriched in trace elements, precious metals and other elements such as Mn, Co, Ni, Cu, Zn, Ga, Ge, As, Se, Ag, Sb, Te, Au, Pb and Bi and shows stability under various physicochemical environments [5–8]. Therefore, pyrite can effectively record the evolution of hydrothermal fluids and gold enrichment mechanism in gold deposits [9–11]. Pb isotope signatures of ore minerals serve as a proxy for the source(s) of the principal ore constituents. As a result, Pb isotope analysis is frequently used in studies of gold mineralization worldwide, often focusing on the analysis of sulphide minerals associated with lode gold mineralization [12–15].

The Jiangnan Orogen (South China) was formed by the collision between the Yangtze and Cathaysia blocks in early Neoproterozoic (Figure 1a) [16]. The orogen is an important gold producing area in China, hosting approximately 250 gold deposits, with a total gold resource over 950 t [17,18]. These gold deposits are mainly hosted in the Neoproterozoic metamorphic clastic rocks (Figure 1b) [17,19]. Previous geochronological investigations indicate that gold mineralization occurred in the the Late Silurian–Devonian, Triassic–Early Jurassic and Middle Jurassic–Early Cretaceous [20–23]. The ore fluid and material sources of these gold deposits in the Jiangnan Orogen are controversial, including: wall rocks and/or deep metamorphic rocks [24–26] and magmatic rocks and/or mantle [22,27–29]. The possibility for multi-stage mineralization overprint and the uncertainty source of ore-forming elements makes the metallogenic process mysterious, but also hinder our understanding of regional gold mineralization.

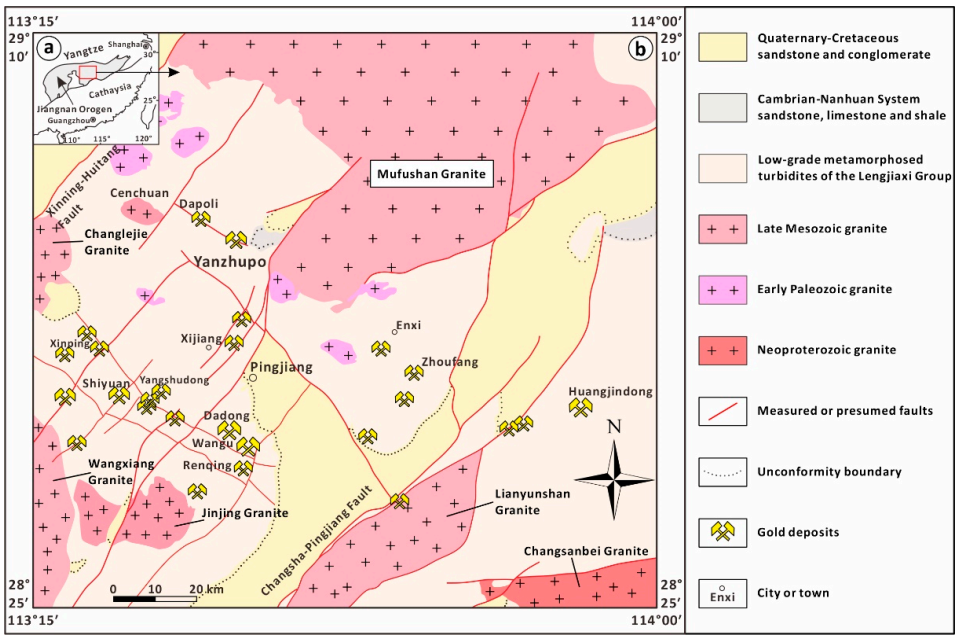

Figure 1. (**a**) Location of Jiangnan Orogen. (**b**) Simplified geological map and distribution of gold deposits in the northeastern Hunan district of the central Jiangnan Orogen (modified from [18]).

In this research, we conducted detailed geological investigations and reported data for pyrite and galena samples from the Yanzhupo gold deposit. We used laser ablation inductively coupled plasma mass spectrometry (LA-ICP-MS) to analyze the trace element compositions of different pyrite generations from Yanzhupo, coupled with backscattered electron (BSE) imaging, and used LA-multi-collector (MC)-ICP-MS to analyze Pb isotopic compositions of galena. Our results provide new insights into the ore material source,

metallogenic process and genesis of Yanzhupo gold deposit, which is helpful to further understand the gold mineralization of the Jiangnan Orogen.

2. Geological Background

2.1. Regional Geology

The Jiangnan Orogen is distributed in an "S" shape in the central part of the South China plate (Figure 1a) and was formed by the collision between the Yangtze and Cathaysia blocks from the late Mesoproterozoic to the early Neoproterozoic [16,30]. It is a significant gold-polymetallic metallogenic belt in China. The regional strata consist primarily of shallow metamorphic pyroclastic rocks and sedimentary rocks from the Neoproterozoic Lengjiaxi Group and Mesoproterozoic Banxi Group [28,31]. After the formation of the Jiangnan Orogen, it underwent several stages of tectonic movements, including early Paleozoic intracontinental orogeny [32,33], the late Triassic collision between the North and South China plates [34,35], and the Middle Jurassic to Late Cretaceous Pacific subduction [36,37]. Magmatic activities are frequent within the orogenic belt, featuring four types of magmatic rocks from the Neoproterozoic, Caledonian (Early Paleozoic), Indosinian (Late Permian to Triassic), and Yanshanian periods (Middle Jurassic to Late Cretaceous) [18].

The newly discovered Yanzhupo gold deposit (reserve: 2.50 t, 2.52 g/t) is located in the northeastern Hunan district of the central Jiangnan Orogen (Figure 1). Exposed stratigraphy in the region consists of the Lengjiaxi Group metamorphic basement, Nanhua System–Cambrian and Cretaceous–Quaternary sedimentary rocks [21,38,39]. The Lengjiaxi Group is composed of shallow metamorphic slate, sandy slate, tuffaceous slate and metamorphic sandstone (zircon U–Pb age: 860–820 Ma) [40,41], which is the main wallrock for most gold deposits in the area (Figure 1b). The sedimentary rocks above the unconformity surface, which overlay the basement are Nanhua System–Cambrian sandstone, limestone and shale and Cretaceous–Quaternary sandstone and conglomerate [7,17].

The Changsanbei granite formed during the Neoproterozoic (zircon $^{207}Pb/^{206}Pb$ age: 929 ± 6 Ma) [42] is the oldest granite in this area. Early Paleozoic granites intruded into the Lengjiaxi Group are scattered in the central and northwestern parts (Figure 1b). During the late Mesozoic, frequent magmatic activities formed numerous granitic complexes (e.g., Mufushan: 158–125 Ma [43]; Lianyunshan: 150–140 Ma [44]; Wangxiang: 151–128 Ma [45]; Jinjing: 166–144 Ma [46]). The dominant structural framework is defined by NE-trending regional folds and various NE- and NW-trending faults. The NE-trending deep faults (e.g., Xinning-Huitang fault and Changsha-Pingjiang fault) restrict the distribution of regional gold deposits (Figure 1b). Meanwhile, the NW-trending faults form the primary ore-hosting structures.

2.2. Deposit Geology

The Lengjiaxi Group exposed in the mining area comprises two formations: the Leishenmiao Formation silty slate and metamorphic siltstone and the Panjiachong Formation metamorphic siltstone and polymict sandstone. All gold orebodies occur within the Leishenmiao Formation of the Lengjiaxi Group. No magmatic rocks are found in the mining area. The NNE-trending (F_2 and F_8) and NNE- to NS-trending (F_7) faults are the primary structure at Yanzhupo, and the auriferous quartz veins are hosted in NW-trending fault fracture zones (Figure 2a) [47].

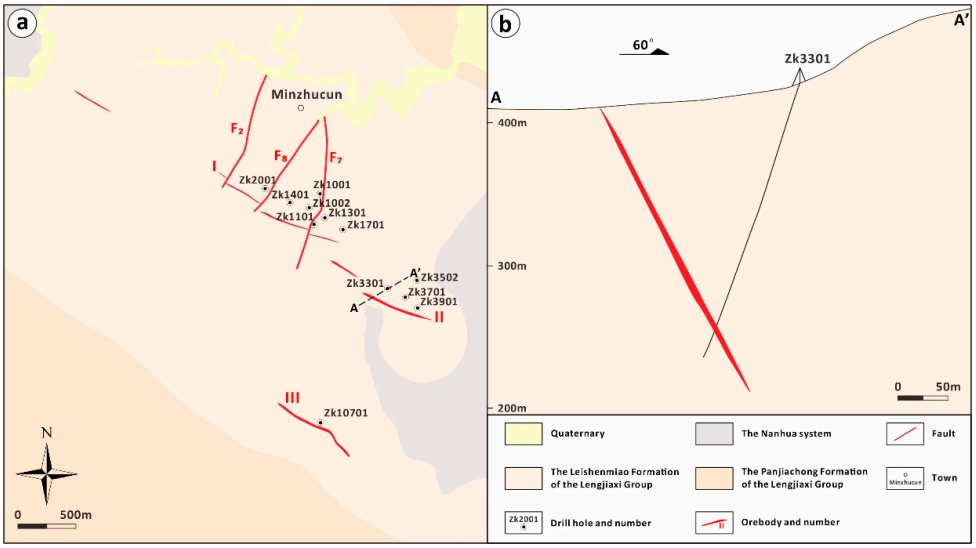

Figure 2. Simplified geologic map (**a**) and representative geological profile (**b**) of the Yanzhupo gold deposit (modified from [47]).

The Yanzhupo gold deposit consists mostly of three gold orebodies (namely I, II and III). These auriferous veins occur in the Lengjiaxi Group slate with NW-striking and NE-dipping at 60–80° (Figure 2). Orebody I is composed of four auriferous quartz veins and has total a lengths of 1250 m, widths of 0.35 to 3.85 m, and gold grades of 0.12–6.3 g/t. Orebody II consists of two auriferous quartz veins with total a lengths of 1200 m, widths of 0.36 to 1.56 m, and gold grades of 0.19–40.7 g/t. Orebody III is located in the southeast of the mining area and is 560 m long and 0.25–0.97 m wide with gold grades of 0.20–6.13 g/t. The alterations include mainly silicification, carbonatization, sericitization and chloritization.

Based on the vein crosscutting relationships and mineral assemblages (Figure 3), the mineralization at Yanzhupo can be divided into three stages: (I) quartz-ankerite-pyrite, (II) quartz-ankerite-chlorite-pyrite-gold, (III) quartz-ankerite-calcite-pyrite. The paragenetic sequence is illustrated in Figure 4. Stage I is characterized by brown and white quartz-ankerite veins (1.0 to 1.5 cm in width; Figure 3a,b). Ore minerals are dominated by subhedral-anhedral pyrite, anhedral chalcopyrite and minor galena (Figure 4). Pyrite grains (0.2–2.0 mm) are made up of light yellow rims (Py1a) and porous cores (Py1b), and the pores of cores are filled with abundant tiny galena and chalcopyrite (Figure 3d,e). Chalcopyrite is mainly found in the quartz-ankerite veins or with pyrite (Figure 3d,e). Stage II represents the main Au mineralization stage and is marked by gray-white quartz-ankerite-chlorite veins (0.5 to 5.0 cm in width) cutting Stage I veins (Figure 3a,c). Ore minerals include abundant pyrite, common chalcopyrite, galena, sphalerite, arsenopyrite, and minor bismuth, tetrahedrite, and native gold (Figure 4). Subhedral-anhedral pyrite grains (20–500 μm) aggregate into irregular lumps or veinlets in quartz-ankerite-chlorite veins, and coexist with galena, chalcopyrite, tetrahedrite and sphalerite (Figure 3f–i). Moreover, some pyrite grains contain an overgrowth region with clear boundary and about 20 μm width (Figure 3g). Euhedral-subhedral arsenopyrite grains occur in veins and host rocks and coexist with native gold (Figure 3h). Native gold grains (average fineness: 897.3) are highly variable in size (<5 to 40 μm), and mainly coexist with arsenopyrite, with a small amount occurring in quartz-ankerite-chlorite veins (Figure 3h). Gold grain shapes are dominantly sub-rounded and angular, with minor irregular shapes associated with filling the fractures in arsenopyrite (Figure 3h). Chalcopyrite interweaves with galena containing bismuth and sphalerite (Figure 3i), and coexists with euhedral apatite (100–400 μm; Figure 3j). Stage III is characterized by quartz-ankerite-calcite veins (0.5 to 1.0 cm in width) cutting Stages I and II veins (Figure 3b,c). Pyrite grains are subhedral to anhedral (0.1–1.0 mm)

and coexist with quartz, ankerite and calcite (Figure 3k). Minor apatite grains (0.2–1.0 mm) occur in quartz-ankerite-calcite veins and partially enclose galena (Figure 3l).

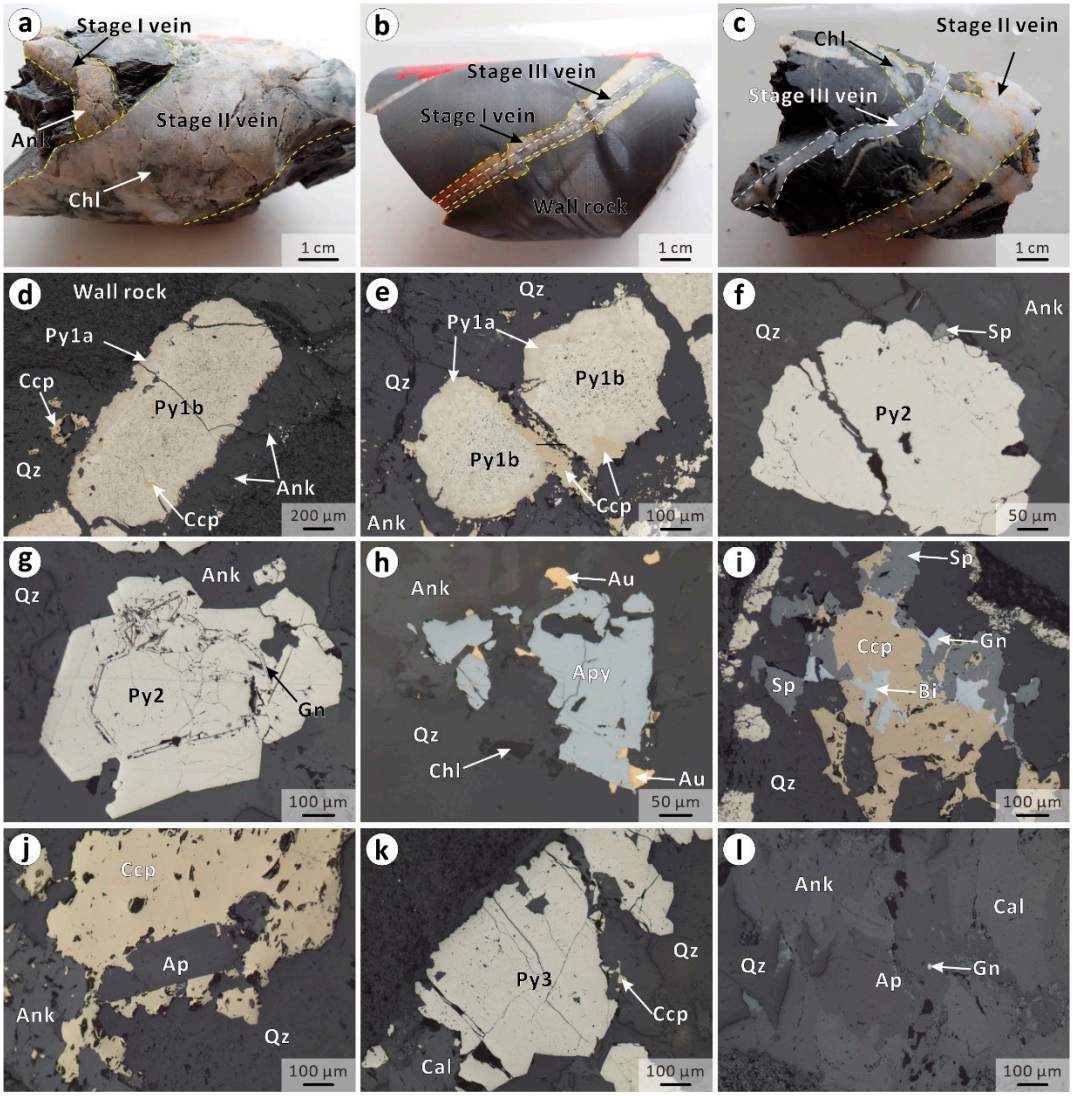

Figure 3. Macro-geological characteristics (**a**–**c**) and ore compositions (**d**–**l**) of the Yanzhupo gold deposit. (**a**) quartz-ankerite-pyrite vein (Stage I) is cut by quartz-ankerite-chlorite-pyrite-gold vein (Stage II); (**b**) quartz-ankerite-calcite-pyrite vein (Stage III) cuts quartz-ankerite-pyrite vein (Stage I); (**c**) quartz-ankerite-chlorite-pyrite-gold vein (Stage II) is cut by quartz-ankerite-calcite-pyrite vein (Stage III); (**d**) pyrite (Py1a at the rim and Py1b at the core) and chalcopyrite in the quartz-ankerite vein (Stage I); (**e**) porous core Py1b and brighter rim Py1a (Stage I); (**f**) pyrite (Py2) and sphalerite occur in the quartz-ankerite-chlorite vein (Stage II); (**g**) pyrite with an overgrowth region and galena occur in the quartz-ankerite-chlorite vein (Stage II); (**h**) arsenopyrite coexists with native gold (Stage II); (**i**) chalcopyrite, galena and sphalerite coexist with bismuth (Stage II); (**j**) chalcopyrite and apatite occur in the quartz-ankerite-chlorite vein (Stage II); (**k**) pyrite (Py3) and chalcopyrite coexist with quartz and calcite (Stage III); (**l**) apatite and galena coexist with ankerite, calcite and quartz (Stage III). Py-pyrite; Ccp-chalcopyrite; Qz-quartz; Ank-ankerite; Gn-galena; Apy-arsenopyrite; Chl-chlorite; Au-native gold; Sp-sphalerite; Bi-bismuth; Ap-apatite; Cal-calcite.

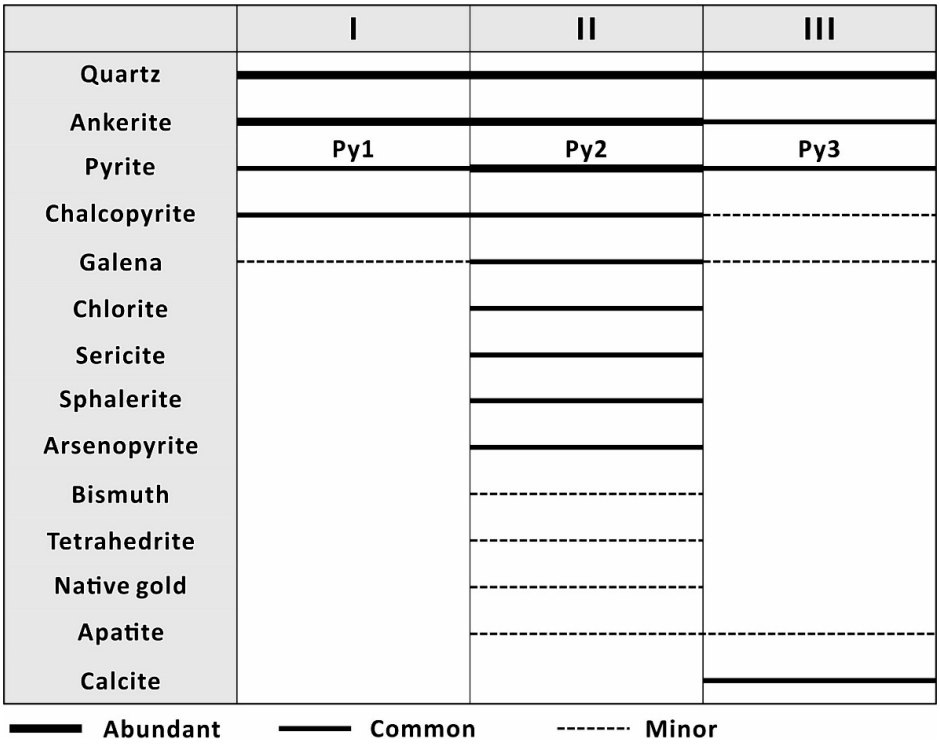

Figure 4. Mineral paragenetic sequence for the Yanzhupo gold deposit.

3. Sampling and Analytical Methods

3.1. Sampling

In this study, we conducted core logging for six drill cores (ZK1001, ZK1002, ZK3301, ZK3502, ZK3701, and ZK3901), collected 103 sulfides-bearing samples and conducted detailed petrographic descriptions on 38 polished blocks. Accordingly, pyrite grains in typical samples (ZK1001-58, ZK1002-36, ZK3502-13, ZK3502-40, ZK3502-44 and ZK3701-18) of three stages (I, II and III) were selected for in-situ LA-ICP-MS trace elements. Because galena grains of Stages I and III are too small, in-situ LA-MC-ICP-MS Pb isotope analyses were completed on the Stage II galena grains (ZK1001-47 and ZK1001-63). Detailed descriptions of samples for experimental analysis are listed in Table 1.

Table 1. Locations and mineral features of analyzed samples from the Yanzhupo gold deposit.

Sample Number	Sampling Location	Ore Stage	Mineral Assemblage
ZK1001-47	487.6 m level	Stage II	Pyrite + chalcopyrite + galena + sphalerite
ZK1001-58	638.9 m level	Stage III	Pyrite + chalcopyrite
ZK1001-63	711.1 m level	Stage II	Pyrite + chalcopyrite + galena + sphalerite + tetrahedrite + bismuth
ZK1002-36	256.1 m level	Stage III	Pyrite + chalcopyrite + galena
ZK3502-13	114.2 m level	Stage I	Pyrite + chalcopyrite + galena
ZK3502-40	356.2 m level	Stage II	Pyrite + chalcopyrite + galena + sphalerite
ZK3502-44	396.6 m level	Stage II	Pyrite + chalcopyrite + galena + sphalerite
ZK3701-18	113.8 m level	Stage I	Pyrite + chalcopyrite + galena

3.2. LA-ICP-MS Pyrite Trace Element Analysis

Pyrite LA-ICP-MS trace-element analysis was completed at the Guangzhou Tuoyan Detection Technology Co., Ltd. (Guangzhou, China). The laboratory employed a New Wave Research 193 nm ArF excimer laser ablation device in conjunction with Thermo Scientific iCap-RQ quadrupole inductively coupled plasma mass spectrometer (ICP-MS).

The excimer laser generator produces a deep ultraviolet beam, which is focused on the sample's surface using a homogenization optical path. The laser beam has a spot diameter of 35 μm, a frequency of 6 Hz, and an energy density of 3.5 J/cm^2. Helium serves as the carrier gas, while argon acts as the compensation gas to adjust sensitivity during laser ablation.

During the in-situ testing of trace element content and the treatment of pyrite microareas, glass standard materials NIST SRM610, MASS-1, and standard pyrite samples (Fe 46.55 wt.%, S 53.45 wt.% [48]) are utilized for multi-external and single internal standard corrections [49,50]. The proportional reference material SRM 612 is used as the monitoring sample [51,52]. Each time-resolved analysis dataset includes approximately 40 s of blank signal and 45 s of sample signal. The offline processing of analytical data, which includes sample and blank signal selection, instrument sensitivity drift correction, and element content calculation, is performed using the 3D Trace Elements DRS mode of the Iolite V 1.4 software [53,54].

3.3. LA-MC-ICP-MS Galena Pb Isotope Analysis

In situ Pb isotope analyses of galena were conducted using a Neptune Plus MC-ICP-MS (Thermo Fisher Scientific, Bremen, Germany), equipped with a Geolas HD excimer ArF laser ablation system (Coherent, Göttingen, Germany) at Wuhan SampleSolution Analytical Technology Co., Ltd, Wuhan, China. Helium was employed as the carrier gas for the ablation cell in the laser ablation system, and it was combined with argon (makeup gas) after the ablation cell. The spot diameter varied from 44 to 90 μm based on Pb signal strength. The pulse frequency ranged from 4 to 10 Hz, however the laser fluence remained constant at ~5 J/cm^2. A new device for signal smoothing and mercury removal was used downstream from the sample cell to effectively eliminate short-term signal variations and remove mercury from the background and sample aerosol particles [55]. The mass spectrometer Neptune Plus is equipped with nine Faraday cups, which can receive ^{208}Pb, ^{207}Pb, ^{206}Pb, ^{204}Pb, ^{205}Tl, ^{203}Tl, and ^{202}Hg signals using static mode. Single-label Tl solution is introduced by membrane dissolution (Aridus II), mixed with laser ablation aerosol particles and then enters ICP, and the real-time instrument mass fractionation correction of Pb isotope is completed by using the ratio of ^{205}Tl/^{203}Tl. Because the mass fractionation behavior of Tl and Pb in ICP is not consistent, two sulfide standard samples, MASS-1(USGS standard sample) and Sph-HYLM (sphalerite, laboratory internal standard sample), are used to determine the mass fractionation relationship between Tl and Pb, and an optimized ^{205}Tl/^{203}Tl ratio with matched matrix is obtained. The new ratio of ^{205}Tl/^{203}Tl replaces the natural ratio of ^{205}Tl/^{203}Tl, and is used for the subsequent Pb isotope analysis of actual sulfide samples. In addition, the residual ^{204}Hg was obtained by monitoring the ^{202}Hg signal and using the natural ratio of ^{202}Hg/^{204}Hg (0.2301). The instrument mass fractionation of ^{202}Hg/^{204}Hg is corrected by Tl isotope, and it is assumed that the fractionation factors of Hg and Tl are the same. As an external standard, sphalerite standard Sph-HYLM is used to monitor and analyze the precision and accuracy. The obtained accuracy is estimated to be equal to or better than ±0.2‰ for ^{208}Pb/^{204}Pb, ^{207}Pb/^{204}Pb and ^{206}Pb/^{204}Pb compared to the solution value by MC-ICP-MS, with a typical precision of 0.4‰ (2σ) [56]. All the analysis data were processed by the professional isotope data processing software "Iso-Compass" [57].

4. Results

4.1. The Yanzhupo Pyrite Types and Internal Textures

Pyrite is the primary sulfide mineral in Stage I, Stage II and Stage III veins. Petrographic observations and back-scattered electron (BSE) imaging revealed six generations

of pyrite (Figure 5). Pyrite from Stage I veins consists of two generations: bright rims (Py1a; Figure 5a–c) and porous cores (Py1b) dissolving Py1a (Figure 5a–c). The dissolved residual Py1a and abundant inclusions (galena and chalcopyrite) can be found in Py1b (Figure 5a–c). Three distinct generations of pyrite (Py2a, Py2b and Py2c) are recognized in the Stage II veins. Py2a, with homogenous textures and rare or no sulfide inclusions, commonly occurs as pyrite core (Figure 5d–f). Py2b replaces Py2a and occurs as subhedral to anhedral overgrowth with oscillatory zoning around residual Py2a (Figure 5d–f). The oscillatory zoning of Py2b is gradually clear from the cores to rims, and the obvious bright band in BSE image is consistent with the overgrowth band seen under optical microscope (Figures 3g and 5d–f). Py2c, with homogenous textures, overgrows around Py2b (Figure 5d–f). Pyrite (Py3) from Stage III veins is texturally homogenous under BSE imaging (Figure 5g–i).

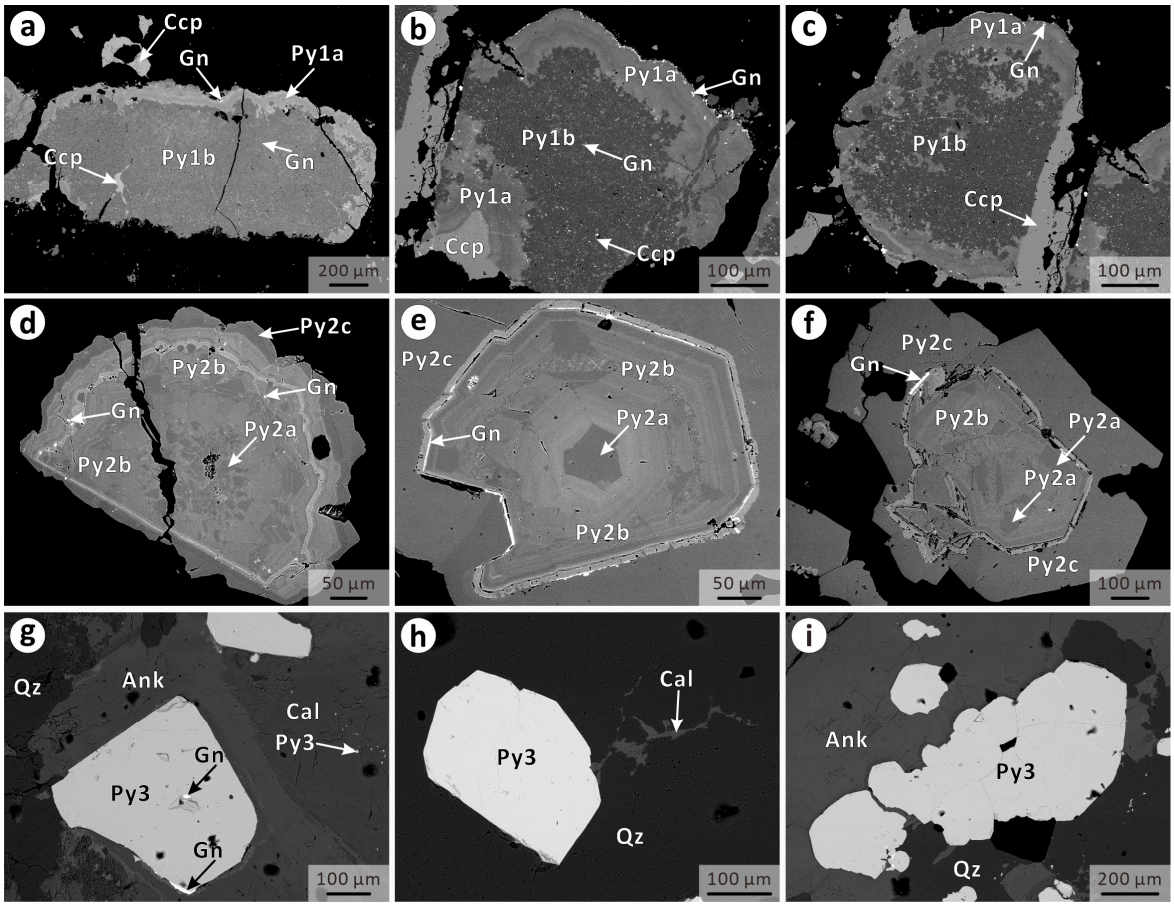

Figure 5. Back-scattered electron (BSE) images of typical pyrite grains of different generations. (**a**–**c**) pyrite grains from Stage I veins consist of bright rims (Py1a) and porous cores (Py1b) and tiny galena and chalcopyrite are filled in the voids of Py1b, and residual Py1a can be seen in Py1b; (**d**–**f**) three distinct generations of pyrite are recognized in the Stage II veins: homogenous Py2a, Py2b with oscillatory zoning (including an obvious bright band) and homogenous Py2c; (**g**–**i**) homogenous pyrite grains (Py3) from Stage III veins. Py-pyrite; Ccp-chalcopyrite; Gn-galena; Qz-quartz; Ank-ankerite; Cal-calcite.

4.2. LA-ICP-MS Trace Element Compositions of Pyrite

A total of 119 LA-ICP-MS spot analyses were conducted on various generations of pyrite from the Yanzhupo deposit, with 13, 6, 12, 50, 25 and 13 spots on Py1a, Py1b, Py2a, Py2b, Py2c and Py3, respectively. Trace element compositions are listed in Supplementary Table S1 and illustrated in Figure 6. The element composition of pyrite varies in a regular manner across the three stages. In general, pyrite grains in Stage I are rich in trace elements,

followed by pyrite grains in Stage II, and pyrite grains in Stage III are poor in trace elements.

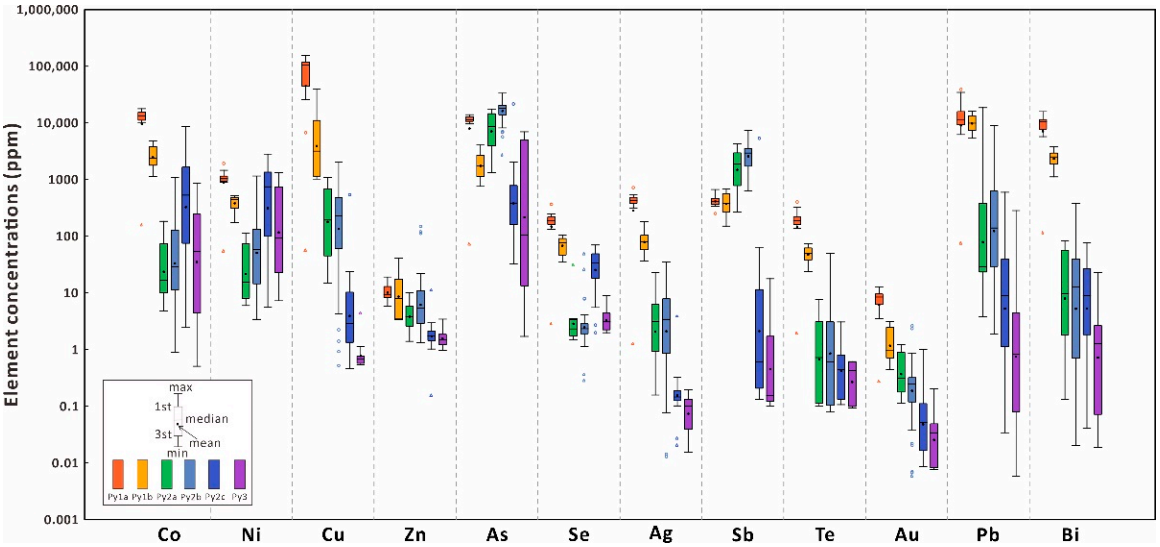

Figure 6. Concentration boxplot showing selected trace element concentrations of Py1 to Py3 from Yanzhupo.

Py1a contains highest Co (avg. 12751 ppm), Ni (avg. 1055 ppm), Cu (avg. 89668 ppm), Zn (avg. 10.7 ppm), Se (avg. 216 ppm), Ag (avg. 421 ppm), Te (avg. 199 ppm), Au (avg. 7.83 ppm), Pb (avg. 14488 ppm) and the second highest As (avg. 10973 ppm) contents among six generations of pyrite, with lower Au/Ag ratios (avg. 0.035). Compared with Py1a, trace elements in Py1b are generally decreased, with lower Co (avg. 2744 ppm), Ni (avg. 405 ppm), Cu (avg. 9658 ppm), As (avg. 2005 ppm), Se (avg. 72.3 ppm), Ag (avg. 88.4 ppm), Te (avg. 50.3 ppm), Au (avg. 1.45 ppm), Pb (avg. 10431 ppm) contents and Au/Ag ratios (avg. 0.019). From Py2a to Py2c, the average contents of Co, Ni and Se gradually increased from 50.0 ppm, 37.5 ppm and 11.9 ppm to 1239 ppm, 800 ppm and 35.5 ppm, respectively. The contents of Zn, As, Sb and Pb and Au/Ag ratios first increase and then decrease from Py2a to Py2c. Py2b contains highest As (avg. 17827 ppm) and Sb (avg. 2863 ppm) among six generations of pyrite. Py2c has lower concentrations of Cu (avg. 37.2 ppm), Ag (avg. 1.45 ppm), Te (avg. 1.43 ppm), Au (avg. 0.157 ppm) and Bi (avg. 17.5 ppm) than Py2a and Py2b. Py3 has significantly lower Cu (avg. 1.77 ppm), Sb (avg. 3.68 ppm), Au (avg. 0.084 ppm), Pb (avg. 25.6 ppm) and Bi (avg. 3.09 ppm) concentrations than Py1 and Py2.

4.3. LA-MC-ICP-MS In-Situ Pb Isotopes of Galena

A total of 14 in-situ Pb isotopes analyses were performed on the Stage II galena grains from ZK1001-47 (n = 7) sample and ZK1001-63 (n = 7) sample. The Pb isotope compositions are presented in Supplementary Table S2 and shown in Figure 7. These samples have $^{208}Pb/^{204}Pb$, $^{207}Pb/^{204}Pb$ and $^{206}Pb/^{204}Pb$ values of 37.768–37.807, 15.649–15.656 and 17.852–17.863 respectively. In the $^{207}Pb/^{204}Pb$-$^{206}Pb/^{204}Pb$ cross-plot, the data points are gathered near the upper crust line.

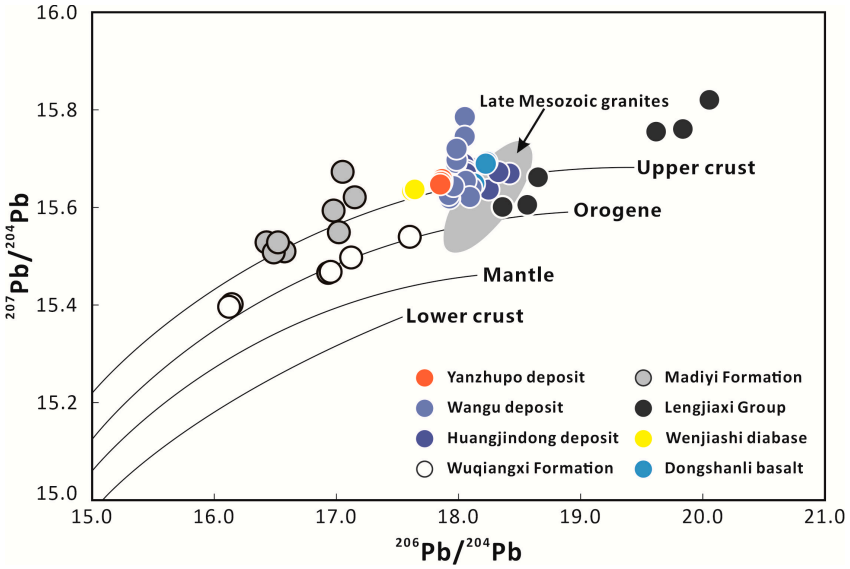

Figure 7. The $^{207}Pb/^{204}Pb$-$^{206}Pb/^{204}Pb$ cross-plot showing the Pb isotope compositions of galena in Stage II veins of the Yanzhupo deposit (modified after [58]). Data sources: Wangu and Huangjindong deposits [17,25]; Wenjiashi diabase and Dongshanli basalt [59]; Late Mesozoic granites [60]; Banxi Group (Wuqiangxi and Madiyi Formation) and Lengjiaxi Group [61].

5. Discussion

5.1. Trace Element Occurrence in Pyrite

Pyrite is a sink for many trace elements, and these trace elements are incorporated into pyrite in different ways: (1) micro- to nano-sized mineral inclusions, (2) solid solution within the crystal lattice [5,62,63]. The relationship between As and Au in pyrite has been extensively reported in many hydrothermal Au deposits [2,64–66], focusing on the occurrence of gold in pyrite and a key role of As to facilitate Au into pyrite [67,68]. Au and As contents of the Yanzhupo pyrite fall below the gold solubility line (Figure 8a), indicating that invisible gold is incorporated into the pyrite lattice. However, the lack of correlation between As and Au implies the weak influence of As on the absorption of Au in the Yanzhupo deposit [69]. Au positively correlates with the Cu content in the Yanzhupo pyrite (Figure 8b; R^2 = 0.82), indicating that the presence of elemental combination of Au-Cu and coupled substitution of Au^{3+} with Cu^{+} for Fe^{2+} (Au^{3+} + Cu^{+} = $2Fe^{2+}$) [70], which requires oxidation fluid environment in the Yanzhupo deposit [71]. As usually enters the pyrite lattice via substitution of S^{-} by As^{-} or Fe^{2+} by $As^{2+/3+}$ [72]. In the relatively oxidizing environment of Yanzhupo, the substitution of Fe^{2+} by $As^{2+/3+}$ is most likely to occur [65,72].

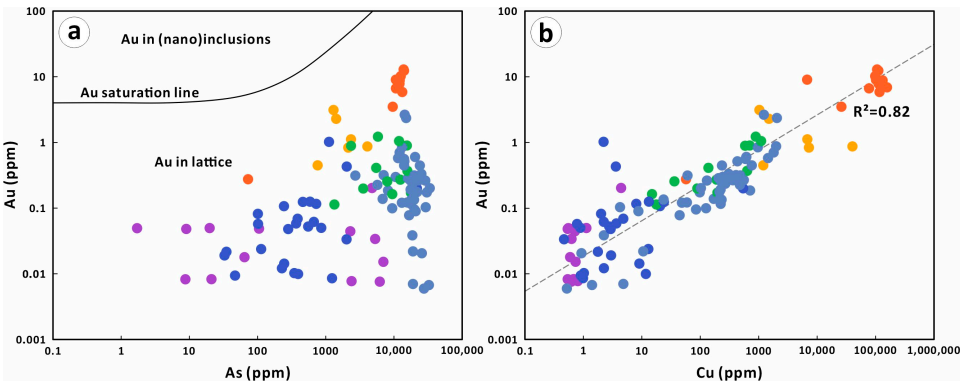

Figure 8. Bivariate plots of trace elements in Py1 to Py3 from Yanzhupo. (**a**) Au vs. As. (**b**) Au vs. Cu.

LA-ICP-MS time-resolved depth-profiles can also provide useful information on the trace element occurrence in pyrite [73]. Co and Ni are readily incorporated into the pyrite lattice via the replacement of Fe [65,74]. The smooth and flat time-resolved depth-profiles of Co, Ni, As for most Yanzhupo pyrite show that they likely occur as solid solution in pyrite (Figure 9). In Py1a, abundant elements (e.g., Pb, Bi, Cu, Ag, Te, Se and Au) may enter the lattice of pyrite based on the smooth and flat time-resolved depth-profiles (Figure 9a). The Pb-Bi and Cu spectral peaks in Py1b indicate the presence of Pb-Bi- and Cu-bearing mineral inclusions (Figure 9b), which is consistent with abundant tiny galena and chalcopyrite in Py1b (Figure 5a–c). It is worth noting that Sb may occur as solid solution in Py1b, Py2a and Py2b based on the smooth and flat time-resolved depth-profiles (Figure 9b–d). Pb-Bi-Ag-, Cu- and Zn- bearing mineral inclusions can be identified from the Pb-Bi-Ag, Cu and Zn spectral peaks in Py2a and Py2b (Figure 9c,d). Meanwhile, the Pb-Bi-Sb-bearing mineral inclusions may appear in Py2c and Py3 (Figure 9e,f), and local signal peaks of Co and Ni in Py3 reflect the occurrence of Co-Ni-bearing mineral inclusions (Figure 9f).

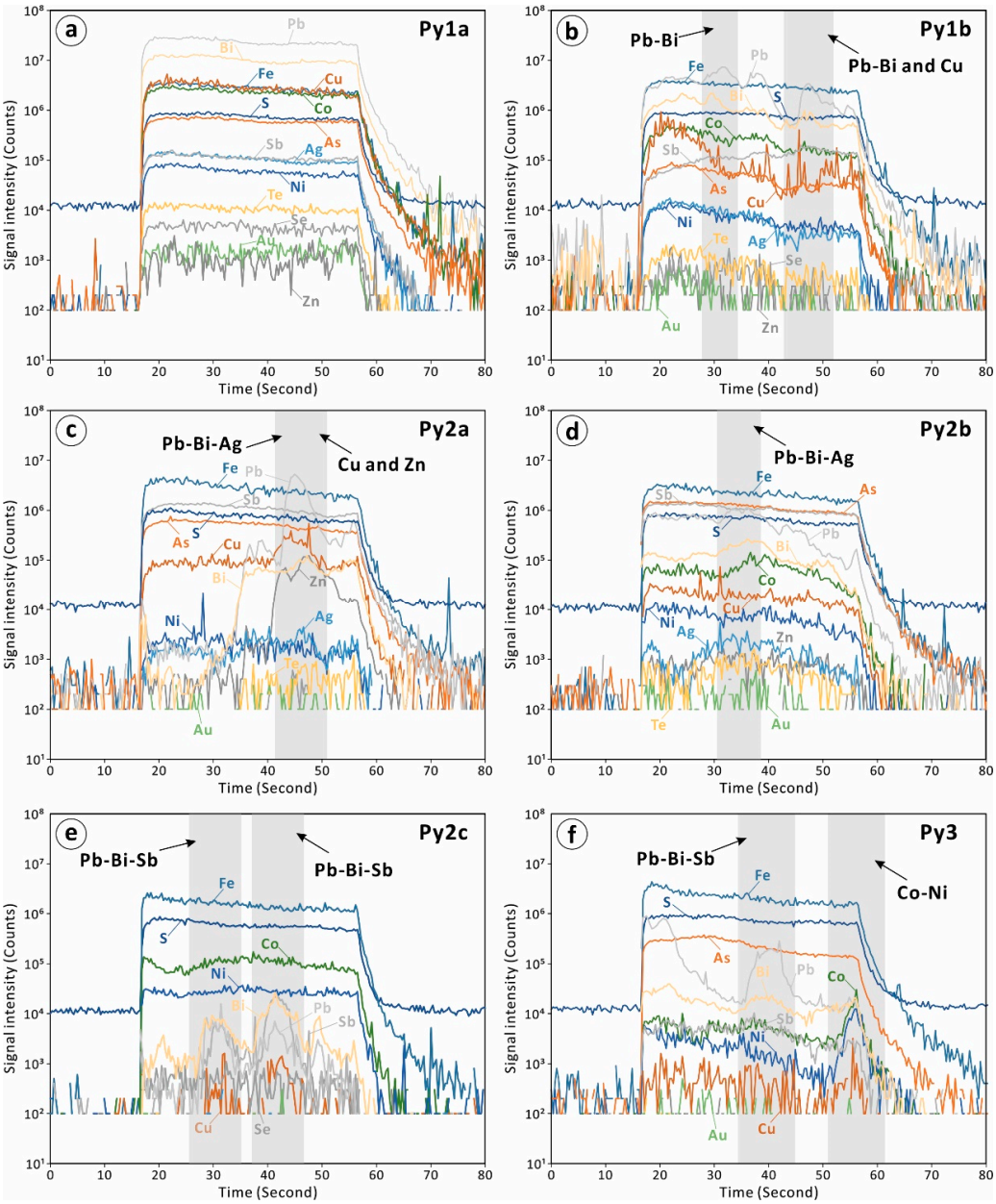

Figure 9. Representative time-resolved depth-profiles of the different types of pyrite in Yanzhupo (**a**–**f**).

5.2. Ore Source

Previous studies on many gold deposits in the northeastern Hunan district have confirmed the complexity and diversity of gold sources, involving metamorphic sedimentary rocks [75,76], granitic magma [8,77], mantle [78] and mixed sources [7,79]. For example, the Tuanshanbei gold deposit is a product of two temporally distinct events (415.1 ± 2.1 Ma and 234.3 ± 1.1 Ma), with gold derived from Neoproterozoic metasedimentary basement rocks (Cangxiyan Group) [80]. The Jinji gold deposit (397.8 ± 14.2 Ma) is considered as a gold deposit related to granitic magma [77]. The Xiaojiashan gold mineralization (216.9 ± 1.1 Ma) was likely associated with early metamorphism and late magmatic-hydrothermal overprinting [7]. Furthermore, the ore sources of the Wangu gold deposit (142–130 Ma [17]) and Huangindong gold deposit (129.7 ± 7.4 Ma [81]) were provided by extensive granitic magmatism [22,82].

In general, the Pb isotope composition is unaffected by physical, chemical or biological processes, and it stays generally constant during mineral precipitation and mineralization [83,84]. Because sulfides have a low proportion of U and Th, their Pb isotope compositions are mostly influenced by the nature of the source location, hence Pb isotopes are frequently used to trace the origin of ore-forming elements in deposits [85]. In the $^{207}Pb/^{204}Pb$-$^{206}Pb/^{204}Pb$ cross-plot, the Yanzhupo Stage II galena samples plot close to the upper crust evolution line, indicating possible crustal origin (Figure 7) [58]. Furthermore, the Pb isotopic features of the Yanzhupo deposit are comparable to the Wangu deposits [17,25], but distinct from those in the Wenjiashi diabase and Dongshanli basalt [59], Late Mesozoic granites [60], Banxi Group (Wuqiangxi and Madiyi Formation) and Lengjiaxi Group [61], suggesting that the Yanzhupo Stage II ore-forming components, similar to the Wangu gold deposit, may have sourced from deep upwelling granitic magma [22].

Pyrite chemical compositions can also provide key information for ore and fluid source in hydrothermal systems [86–88]. Py2c and Py3 (Figure 9a–f) have similar trace element compositions, while lacking systematic differences, suggesting the consistency of their sources (Figure 6). In addition, we have not found traces of multi-stage hydrothermal activities in the Yanzhupo gold deposit. Therefore, the ore-forming materials of the Yanzhupo gold deposit may come from deep granitic magma. Compared to pyrite grains in Stages II and III, Stage I pyrite samples contain a high concentration of trace elements (e.g., Co, Ni, Cu, Se, Te and Au). Rich metal elements may come from the deep ancient basement, which is the result of fluid-mineral interactions [89,90]. The widespread development of the Cu-Pb-Zn-Co polymetallic metallogenic system related to the ancient basement (maybe Lianyunshan Group) in the northeastern Hunan district [91–93], as well as previous studies on trace elements in the ancient crystalline basement support this argument [94].

5.3. Ore-Forming Process

Pyrite Co/Ni ratio is sensitive to physicochemical conditions and can be used to determine its origin [95–97]. Generally, pyrite with Co/Ni < 1 is attributed to sedimentary origin, while hydrothermal pyrite usually has Co/Ni > 1 [62,87]. Furthermore, hydrothermal pyrite with Co/Ni ratios less than 1 may be caused by fluid-mineral interactions [98,99]. Most Co/Ni data points of the Yanzhupo pyrite are 0.1–10 (Figure 10a), demonstrating their hydrothermal origin with the influence of fluid-mineral interactions, which is also supported by their coexistence with hydrothermal minerals (quartz, ankerite, chlorite and calcite) and wall rock alterations in Yanzhupo. Pyrite of hydrothermal origin can be used to constrain the Yanzhupo ore-forming process [9–11].

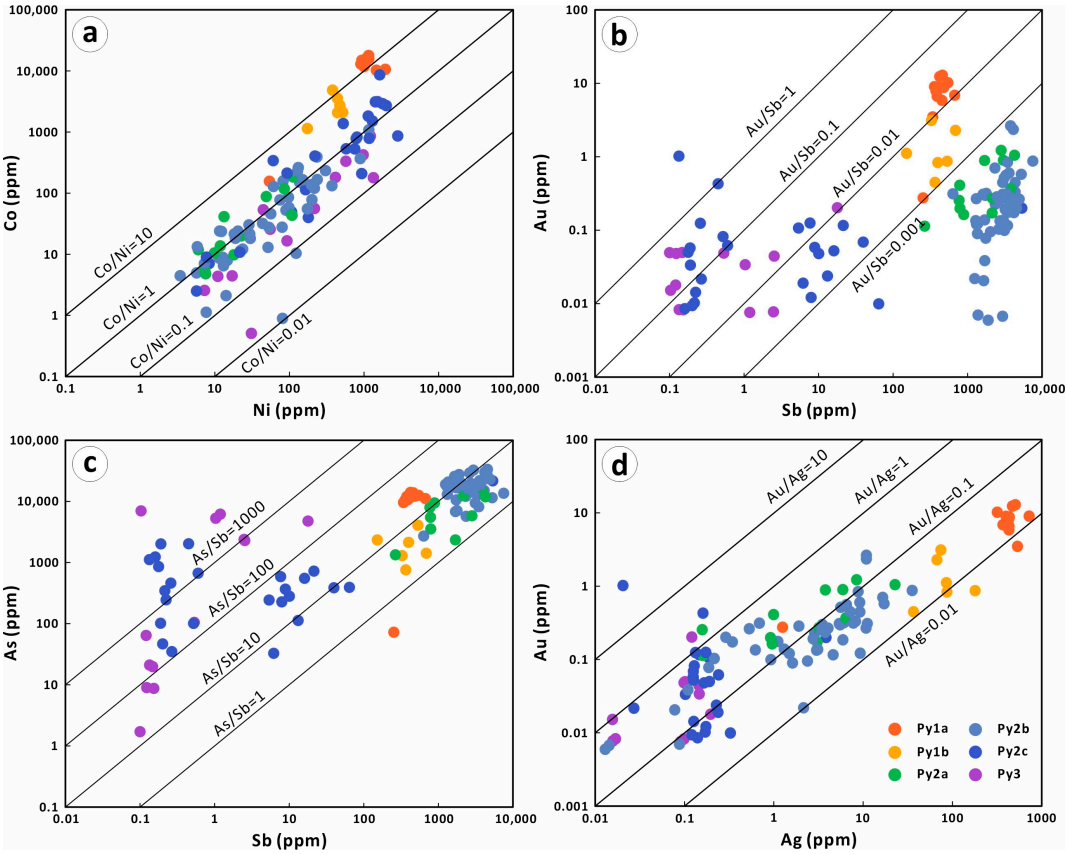

Figure 10. Bivariate plots of trace elements in Py1 to Py3 from Yanzhupo. (**a**) Co vs. Ni. (**b**) Au vs. Sb. (**c**) As vs. Sb. (**d**) Au vs. Ag.

Py1a was first precipitated in Yanzhupo from hydrothermal-magmatic fluid, which extracted a lot of metal elements from ancient metamorphic basement through fluid-mineral interactions. Compared with pyrite in other stages, the excessive Cu concentrations render Py1a more yellow. High-temperature fluids may contribute to the Cu enrichment of Py1a, because the solubility of Cu in Cl-bearing hydrothermal fluids increases with higher fluid temperature [100,101]. Higher temperatures promotes a large number of metal elements (such as Cu, Co and Ni) to enter pyrite, resulting in significant lattice defects and vacancies [102,103], which made the unit cell unstable and was beneficial to the combination of heavier and larger elements, such as Au [2,104]. Py1a, which is enriched in Au-Cu, formed the primary gold precipitation in the Yanzhupo mining area.

Py1b is characterized by the development of numerous voids filled with tiny chalcopyrite and galena (Figure 5a–c) and the content of trace elements generally decreased compared with Py1a (Figure 6). More importantly, the reaction front between Py1b and Py1a is sharp and curvilinear and residual Py1a appears in Py1b (Figure 5a–c). These characteristics suggest coupled dissolution-reprecipitation (CDR) reactions [105], representing that fluids dissolved earlier Py1a and then reprecipitated as Py1b. The changes of physicochemical conditions of hydrothermal fluids, such as the increase of temperature, salinity and fO_2, are very important to drive the dissolution of primary pyrite [106]. The gradual cooling of ore fluids and the absence of gypsum salt layer in Yanzhupo reject the possibility of Py1a dissolving due to salinity and temperature increase. The CDR reactions caused by oxidizing fluids have been reported in several studies [107–109]. As discussed above, the Yanzhupo ore-forming fluids have high oxygen fugacity, and it is very possible that oxidized ore fluid itself drove CDR reactions. The CDR reactions in the late Stage I are crucial to the redistribution and re-enrichment of gold plus other trace metals:

Py1a + fluids (Cu^{2+}, Zn^{2+}, Pb^{2+}, Bi^{2+})$_{(aq)}$ → Py1b + Ccp + Gn + fluids (Co^{2+}, Ni^{2+}, As^{-}, Se^{2-}, Sb^{-}, Ag^{+}, Au^{+})$_{(aq)}$.

Stage II pyrite grains have delicate zoning related to variations in the As and Sb contents of ore fluids, containing oscillatory-zoned Py2b with higher As and Sb concentrations and darker homogenous Py2a and Py2c with lower As and Sb concentrations (Figures 5d–f and 6; Supplementary Table S1). Sb does not show obvious correlation with Au (Figure 10b), but displays co-enrichment with As (Figures 6 and 10c), which may be related to their similarity in geochemical properties [110–112]. The increase of pH value is an efficient mechanism for As and Pb precipitation into pyrite [111,112]. Therefore, the formation of Py2a and Py2b may be related to the increase of fluids pH and oscillatory zoning in Py2b reflects periodic and repetitive changes in pH of ore fluids [113]. In the Yanzhupo deposit, the absence of sulfates and hematite suggest that H_2S was the predominant sulfur species in the ore fluid during pyrite formation [114]. As mentioned above, chlorite and sericite occur in Stage II veins. Hence, the increasing pH of the Stage II ore fluids may be influenced by sulfidation of the wall rocks, because this process can lead to the loss of H_2S [109,115]. The lower As and Pb contents in Py2c seem to express decreasing pH, but the more reasonable explanation may be that the formation of Py2a and Py2b consumed a lot of As and Pb from ore fluids. The CDR reactions released loads of primary gold in Py1a, which mainly migrates as the $Au(HS)_2^-$ and $Au(HS)S_3^-$ complexes [116,117]. Thus, the destabilization of gold with sulfur complexes, caused by the loss of H_2S from the ore fluids during the sulfidation of wall rocks, is the most likely mechanism for gold deposition [115], which is supported by abundant native gold grains in the Stage II veins (Figure 3h). In addition, the high fineness (average fineness: 897.3) of native gold generation also confirms the contribution of the sulfidation of wall rocks. This is because Ag is often transported as as chloride complexes ($AgCl_2^-$) [115], and desulfidation of fluid for depositing Stage II pyrite would destroy Au-S complexes but have limited influence on Ag-Cl complexes, contributing to high fineness of Au grains [118]. The markedly different fate of Au compared with Ag in the process also accounts for the increase of Au/Ag from Stage I pyrite to Stage II pyrite (Figure 10d) [67]. With a substantial amount of metal elements deposited in the Stage I and Stage II quartz veins, the barren ore fluids formed homogeneous Py3 under relatively stable conditions.

5.4. Implications for Gold Mineralization

In the northeastern Hunan district, the Early Paleozoic intracontinental orogeny led to extensive metamorphism of gold-rich sedimentary rocks such as the Lengjiaxi Group, the Banxi Group and the Nanhua System to form gold-rich fluids [24,25]. During the Jurassic–Cretaceous period, due to the subduction and rollback of the Paleopacific plate, South China generated extensive NE regional faults and granitic magmatism [119–121]. Magmatic fluids associated with granitic intrusions played a key role in the formation of the gold deposits (e.g., Wangu and Huangjindong deposits) in the northeastern Hunan district [22,27,28,78]. The Yanzhupo gold deposit is close to the Wangu gold deposit (Figure 1b), and they share similar stratigraphic and structural conditions, as well as comparable mineral paragenetic sequence, mineral assemblages, and wall rock alterations [17]. Therefore, we conclude that the Yanzhupo gold deposit, similar to the Wangu gold deposit, is a magmatic-hydrothermal gold deposit, which is consistent with the Pb isotope analysis results (Figure 7). Furthermore, based on the varying gold sources influenced by different tectonic environments, we can speculate that the Yanzhupo gold deposit may have formed during the Yanshanian period (Middle Jurassic to Late Cretaceous), similar to the Wangu and Huangjindong deposits, although we lack precise data on the age of gold mineralization.

By studying ubiquitous pyrite in all stages of the Yanzhupo deposit, we monitor the properties and fluctuations of the chemical conditions of the ore fluids and have proposed the following model for the redistribution and re-enrichment of gold and other trace metals: (early Stage I) Cu-rich Py1a precipitated from the high temperature magmatic fluids, forming primary gold enrichment (Figure 11a); (late Stage I) oxidizing fluids promoted the dissolution of unstable Py1a, released rich metal elements into the fluids again, and reprecipitated porous Py1b poor in trace metals (Figure 11b); (Stage II) due to the fluctuation of the fluid pH value caused by sulfidation of the wall rocks, the delicate zoning pyrite (including Py2a, Py2b and Py2c) and native gold are precipitated from magmatic-hydrothermal fluids (Figure 11c); (Stage III) the barren fluids precipitated homogeneous Py3 in the later stage of mineralization (Figure 11d). Dissolution and reprecipitation replacement of auriferous sulfides is ubiquitous in hypogene gold mineralization systems worldwide [122–124] and is crucial to the redistribution and re-enrichment of gold and other trace metals [125–128]. At the same time, sulfidation of the wall rocks is also an important mechanism of gold deposition [115]. Hence, we propose that the gold resources in the Yanzhupo gold deposit are accumulated under the coupling of two mechanisms.

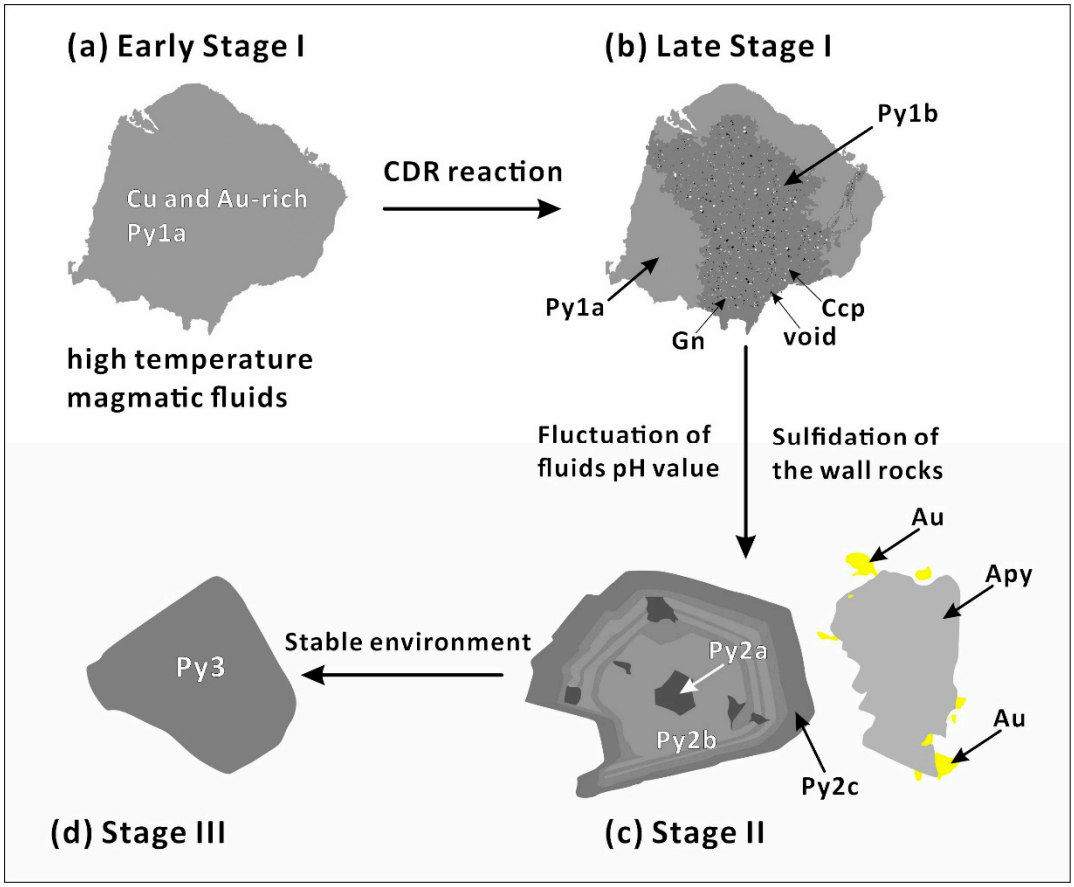

Figure 11. Schematic genetic model for the different types of pyrite from Yanzhupo.

6. Conclusions

The conclusions of this study are as follows:

1. The Yanzhupo deposit alteration and mineralization comprise three stages: (I) quartz-ankerite-pyrite, (II) quartz-ankerite-chlorite-pyrite-gold, (III) quartz-ankerite-calcite-pyrite. Six generations of pyrite were identified in Stage I (Py1a and Py1b), Stage II (Py2a, Py2b and Py2c) and Stage III (Py3).

2. The characteristics of galena Pb isotope and pyrite chemical compositions show that the Yanzhupo deposit ore-forming materials, similar to the Wangu gold deposit, may come from deep upwelling granitic magma.

3. Comprehensive analysis indicates that the Yanzhupo gold deposit may have been associated with magmatic-hydrothermal activity, where CDR reactions and sulfidation of the wall rocks contributed to the enrichment and precipitation of gold.

Supplementary Materials: The following supporting information can be downloaded at: https://www.mdpi.com/article/10.3390/min15010094/s1, Table S1: LA-ICP-MS analyses of differnet types of pyrite from the Yanzhupo gold deposit (ppm); Table S2: In-situ Pb isotope analyses of galena from Stage II veins of the Yanzhupo gold deposit.

Author Contributions: Conceptualization, J.L.; methodology, Z.Z.; software, B.C.; validation, W.W. and B.W.; formal analysis, D.P. and B.W.; investigation, D.P., Q.Z. and Z.L.; resources, J.L. and B.W.; data curation, J.L. and X.W.; writing–original draft preparation, X.W. and Z.Z.; writing–review and editing, X.W., W.W., D.P. and Q.Z.; visualization, Z.Z., Z.L. and Q.X.; supervision, B.C. and Q.X.; project administration, J.L.; funding acquisition, J.L. All authors have read and agreed to the published version of the manuscript.

Funding: This research was funded by the Geological Survey Projects of the China Geological Survey (DD20220969).

Data Availability Statement: All the research data related to this paper have been listed in the manuscript.

Acknowledgments: We are very grateful to the anonymous reviewers for their criticism and constructive comments and suggestions, which helped to significantly improve this paper. We thank Guangzhou Tuoyan Detection Technology Co., Ltd. and Wuhan SampleSolution Analytical Technology Co., Ltd, Hubei, China for their help in the experimental analysis.

Conflicts of Interest: The authors declare no conflict of interest.

References

1. Groves, D.I.; Bierlein, F.P.; Meinert, L.D.; Hitzman, M.W. Iron Oxide Copper-Gold (IOCG) Deposits through Earth History: Implications for Origin, Lithospheric Setting, and Distinction from Other Epigenetic Iron Oxide Deposits. *Econ. Geol.* **2010**, *105*, 641–654. [CrossRef]
2. Deditius, A.P.; Reich, M.; Kesler, S.E.; Utsunomiya, S.; Chryssoulis, S.L.; Walshe, J.; Ewing, R.C. The coupled geochemistry of Au and as in pyrite from hydrothermal ore deposits. *Geochim. Et Cosmochim. Acta* **2014**, *140*, 644–670. [CrossRef]
3. Tanner, D.; Henley, R.W.; Mavrogenes, J.A.; Holden, P. Sulfur isotope and trace element systematics of zoned pyrite crystals from the El Indio Au–Cu–Ag deposit, Chile. *Contrib. Mineral. Petrol.* **2016**, *171*, 33. [CrossRef]
4. Steadman, J.A.; Large, R.R.; Olin, P.H.; Danyushevsky, L.V.; Meffre, S.; Huston, D.; Fabris, A.; Lisitsin, V.; Wells, T. Pyrite trace element behavior in magmatic-hydrothermal environments: An LA-ICPMS imaging study. *Ore Geol. Rev.* **2021**, *128*, 103878. [CrossRef]
5. Deditius, A.P.; Utsunomiya, S.; Reich, M.; Kesler, S.E.; Ewing, R.C.; Hough, R.C.; Walshe, J. Trace metal nanoparticles in pyrite. *Ore Geol. Rev.* **2011**, *42*, 32–46. [CrossRef]
6. Smith, J.W.; Holwell, D.A.; McDonald, I. Precious and base metal geochemistry and mineralogy of the Grasvally Norite-Pyroxenite-Anorthosite (GNPA) member, northern Bushveld Complex, South Africa: Implications for a multi-stage emplacement. *Miner. Depos.* **2014**, *49*, 667–692. [CrossRef]
7. Tan, H.; Shao, Y.; Liu, Q.; Zhang, Y.; Feng, Y.; Zhang, Y.; Sajjad, A.S. Textures, trace element geochemistry and in-situ sulfur isotopes of pyrite from the Xiaojiashan gold deposit, Jiangnan Orogen: Implications for ore genesis. *Ore Geol. Rev.* **2022**, *144*, 104843. [CrossRef]
8. Zhang, Y.; Shao, Y.; Liu, Q.; Zhang, X.; Zhan, Y.; Wang, C.; Wu, H.; Sun, J. Pyrite textures, trace element and sulfur isotopes of Yanlinsi slate-hosted deposit in the Jiangnan Orogen, South China: Implications for gold mineralization processes. *Ore Geol. Rev.* **2022**, *148*, 105029. [CrossRef]
9. Cook, N.J.; Ciobanu, C.L.; Mao, J. Textural control on gold distribution in As-free pyrite from the Dongping, Huangtuliang and Hougou gold deposits, North China Craton (Hebei Province, China). *Chem. Geol.* **2009**, *264*, 101–121. [CrossRef]

10. Ulrich, T.; Long, D.; Kamber, B.; Whitehouse, M. In situ trace element and sulfur isotope analysis of pyrite in a Paleoproterozoic gold placer deposit, Pardo and Clement townships, Ontario, Canada. *Econ. Geol.* **2011**, *106*, 667–686. [CrossRef]
11. Deol, S.; Deb, M.; Large, R.R.; Gilbert, S. LA-ICPMS and EPMA studies of pyrite, arsenopyrite and loellingite from the Bhukia-Jagpura gold prospect, southern Rajasthan, India: Implications for ore genesis and gold remobilization. *Chem. Geol.* **2012**, *326*, 72–87. [CrossRef]
12. Tosdal, R.M.; Wooden, J.L.; Bouse, R.M. Pb isotopes, ore deposits, and metallogenic terranes. In *Application of Radiogenic Isotopes to Ore Deposit Research and Exploration, Reviews in Economic Geology*; Lambert, D.D., Ruiz, J., Eds.; Society of Economic Geologists: Littleton, CO, USA, 1999; Volume 12, pp. 1–28.
13. Potra, A.; Macfarlane, A.W. Lead isotope studies of the Guerrero composite terrane, west-central Mexico: Implications for ore genesis. *Miner. Depos.* **2014**, *49*, 101–117. [CrossRef]
14. Standish, C.D.; Dhuime, B.; Chapman, R.J.; Hawkesworth, C.J.; Pike, A.W.G. The genesis of gold mineralisation hosted by orogenic belts: A lead isotope investigation of Irish gold deposits. *Chem. Geol.* **2014**, *378–379*, 40–51. [CrossRef]
15. Xiong, L.; Zhao, X.; Wei, J.; Jin, X.; Fu, L.; Lin, Z. Linking Mesozoic lode gold deposits to metal-fertilized lower continental crust in the North China Craton: Evidence from Pb isotope systematics. *Chem. Geol.* **2020**, *533*, 119440. [CrossRef]
16. Yan, C.; Shu, L.; Santosh, M.; Yao, J.; Li, J.; Li, C. The Precambrian tectonic evolution of the western Jiangnan Orogen and western Cathaysia Block: Evidence from detrital zircon age spectra and geochemistry of clastic rocks. *Precambrian Res.* **2015**, *268*, 33–60. [CrossRef]
17. Deng, T.; Xu, D.; Chi, G.; Wang, Z.; Jiao, Q.; Ning, J.; Dong, G.; Zou, F. Geology, geochronology, geochemistry, and ore genesis of the Wangu gold deposit in northeastern Hunan Province, Jiangnan Orogen. South China. *Ore Geol. Rev.* **2017**, *88*, 619–637. [CrossRef]
18. Xu, D.; Deng, T.; Chi, G.; Wang, Z.; Zou, F.; Zhang, J.; Zou, S. Gold mineralization in the Jiangnan Orogenic Belt of South China: Geological, geochemical and geochronological characteristics, ore deposit-type and geodynamic setting. *Ore Geol. Rev.* **2017**, *88*, 565–618. [CrossRef]
19. Sun, S.; Yang, L.; Zhang, L.; Wang, J. Origin of Zhengchong gold deposit, northeastern Hunan Province, China: Constraints from sulfur and lead isotopes. *Acta Petrol. Sin.* **2020**, *36*, 1461–1476, (In Chinese with English abstract).
20. Dong, G.J.; Xu, D.R.; Wang, L.S.; Chen, G.H. Determination of mineralization age and tracing of ore bearing fluid source of gold deposits in eastern Hunan—Also on genetic types of deposits. *Geotecton. Et Metallog.* **2008**, *32*, 10, (In Chinese with English abstract).
21. Han, F.B.; Chang, L.; Cai, M.H.; Liu, S.Y.; Zhang, S.-Q.; Chen, Y.; Peng, Z.-A.; Xu, M. Ore-forming epoch of gold deposits in northeastern Hunan. *Miner. Depos.* **2010**, *29*, 563–571, (In Chinese with English abstract).
22. Deng, T.; Xu, D.; Chi, G.; Wang, Z.; Chen, G.; Zhou, Y.; Li, Z.; Ye, T.; Yu, D. Caledonian (Early Paleozoic) veins overprinted by Yanshanian (Late Mesozoic) gold mineralization in the Jiangnan Orogen: A case study on gold deposits in northeastern Hunan, South China. *Ore Geol. Rev.* **2020**, *124*, 103586. [CrossRef]
23. Wang, Z.; Zhang, X.; Liu, Q.; Shao, Y.; Wu, S.; Pan, Z.; Chen, M.; Zhang, Y.; Wu, H. Genesis of the Lishupo gold deposit in the Jiangnan Orogen, NE Hunan (South China): Biotite Ar-Ar, zircon U-Pb ages and H-O-S-Pb isotopic constraints. *Ore Geol. Rev.* **2022**, *145*, 104890. [CrossRef]
24. Liu, A.-L.; Zhang, X.-J.; Ulrich, T.; Zhang, J.; Jiang, M.-R.; Liu, W.-H. Geology, geochronology and fluid characteristics of the Pingqiu gold deposit, Southeastern Guizhou Province, China. *Ore Geol. Rev.* **2017**, *89*, 187–205. [CrossRef]
25. Zhang, L.; Yang, L.-Q.; Groves, D.I.; Liu, Y.; Sun, S.-C.; Qi, P.; Wu, S.-G.; Peng, J.-S. Geological and H-O-S-Pb isotopic constraints on ore genesis, Huangjindong gold deposit, Jiangnan Orogen, southern China. *Ore Geol. Rev.* **2018**, *99*, 264–281. [CrossRef]
26. Wang, J.; Wen, H.; Li, C.; Zhang, J.; Ding, W. Age and metal source of orogenic gold deposits in Southeast Guizhou Province, China: Constraints from Re–Os and He–Ar isotopic evidence. *Geosci. Front.* **2019**, *10*, 581–593. [CrossRef]
27. Li, W.; Xie, G.-Q.; Mao, J.-W.; Zhang, Z.-Y.; Fu, B.; Lu, S. Muscovite $^{40}Ar/^{39}Ar$ and in situ sulfur isotope analyses of the slate-hosted Gutaishan Au–Sb deposit, South China: Implications for possible Late Triassic magmatic-hydrothermal mineralization. *Ore Geol. Rev.* **2018**, *101*, 839–853. [CrossRef]
28. Li, W.; Cook, N.J.; Xie, G.-Q.; Mao, J.-W.; Ciobanu, C.; Fu, B. Complementary Textural, Trace Element, and Isotopic Analyses of Sulfides Constrain Ore-Forming Processes for the Slate-Hosted Yuhengtang Au Deposit, South China. *Econ. Geol.* **2021**, *116*, 1825–1848. [CrossRef]
29. Dai, J.; Xu, D.; Chi, G.; Li, Z.; Deng, T.; Zhang, J.; Li, B. Origin of the Woxi orogenic Au-Sb-W deposit in the west Jiangnan Orogen of South China: Constraints from apatite and wolframite U-Pb dating and pyrite in-situ S-Pb isotopic signatures. *Ore Geol. Rev.* **2022**, *150*, 105134. [CrossRef]
30. Wang, Y.; Zhang, F.; Fan, W.; Zhang, G.; Chen, S.; Cawood, P.A.; Zhang, A. Tectonic setting of the South China Block in the early Paleozoic: Resolving intracontinental and ocean closure models from detrital zircon U-Pb geochronology. *Tectonics* **2010**, *29*, 6. [CrossRef]

31. Wang, Z.Q.; Gao, L.Z.; Ding, X.Z.; Huang, Z.Z. Tectonic Environment of the Metamorphosed Basement in the Jiangnan Orogen and Its Evolutional Features. *Geol. Rev.* **2012**, *58*, 401–413, (In Chinese with English abstract).
32. Wang, Y.; Fan, W.; Zhang, G.; Zhang, Y. Phanerozoic tectonics of the South China Block: Key observations and controversies. *Gondwana Res.* **2013**, *23*, 1273–1305. [CrossRef]
33. Shu, L.S.; Jahn, B.M.; Charvet, J.; Santosh, M.; Wang, B.; Xu, X.S.; Jiang, S.Y. Early Paleozoic depositional environment and intraplate tectono-magmatism in the Cathaysia Block (South China): Evidence from stratigraphic, structural, geochemical and geochronological investigations. *Am. J. Sci.* **2014**, *314*, 154–186. [CrossRef]
34. Liu, J.; Tran, M.-D.; Tang, Y.; Nguyen, Q.-L.; Tran, T.-H.; Wu, W.; Chen, J.; Zhang, Z.; Zhao, Z. Permo-Triassic granitoids in the northern part of the Truong Son belt, NW Vietnam: Geochronology, geochemistry and tectonic implications. *Gondwana Res.* **2012**, *22*, 628–644. [CrossRef]
35. Faure, M.; Lepvrier, C.; Nguyen, V.V.; Vu, T.V.; Lin, W.; Chen, Z. The South China block-Indochina collision: Where, when, and how? *J. Asian Earth Sci.* **2014**, *79*, 260–274. [CrossRef]
36. Mao, J.; Cheng, Y.; Chen, M.; Pirajno, F. Major types and time-space distribution of Mesozoic ore deposits in South China and their geodynamic settings. *Miner. Depos.* **2013**, *48*, 267–294.
37. Zheng, H.; Sun, X.; Wang, P.; Chen, W.; Yue, J. Mesozoic tectonic evolution of the Proto-South China Sea: A perspective from radiolarian paleobiogeography. *J. Asian Earth Sci.* **2019**, *179*, 37–55. [CrossRef]
38. Fu, G.-G.; Xu, D.-R.; Chen, G.-H.; Li, P.-C. New recognitions on geological characteristics of gold ore deposits in northeastern Hunan province, China and new prospecting advances. *Geotecton. Et Metallog.* **2002**, *4*, 416–422, (In Chinese with English abstract).
39. Lu, W.; Sun, J.; Zhou, C.; Guo, A.M.; Peng, W. Source of ore-forming materials and types of ore-forming fluids in yanlinsi gold deposit, Northeastern Hunan. *Acta Geosci. Sin.* **2020**, *41*, 11, (In Chinese with English abstract).
40. Meng, Q.-X.; Zhang, J.; Geng, J.-Z.; Zhang, C.-L.; Huang, W.-C. Zircon U-Pb age and Hf isotope compositions of Lengjiaxi and Baxi Groups in middle Hunan Province: Implications for the Neoproterozoic tectonic evolution in South China. *Geol. China* **2013**, *40*, 191–216, (In Chinese with English abstract).
41. Bai, D.; Jiang, Q.; Li, B.; Jiang, W.; Li, Y. Geochemistry and tectonic implication of the sedimentary rocks in Lengjiaxi Group in northeastern Hunan. *Bull. Geol. Sci. Technol.* **2021**, *40*, 1–13, (In Chinese with English abstract).
42. Wang, X.L.; Zhou, J.C.; Qiu, J.S.; Gao, J.F. Petrogenesis of Neoproterozoic Peraluminous Granites from Northeastern Hunan Province:Chronological and Geochemical Constraints. *Geol. Rev.* **2004**, *50*, 65–76.
43. Ji, W.; Faure, M.; Lin, W.; Chen, Y.; Chu, Y.; Xue, Z. Multiple Emplacement and Exhumation History of the Late Mesozoic Dayunshan–Mufushan Batholith in Southeast China and Its Tectonic Significance: 1. Structural Analysis and Geochronological Constraints. *J. Geophys. Res. Solid Earth* **2018**, *123*, 689–710. [CrossRef]
44. Wang, J.Q.; Shu, L.S.; Santosh, M. Petrogenesis and tectonic evolution of Lianyunshan complex, South China: Insights on Neoproterozoic and late Mesozoic tectonic evolution of the central Jiangnan Orogen. *Gondwana Res.* **2016**, *39*, 114–130. [CrossRef]
45. Jia, D.; Hu, R.; Zhao, J.; Xie, G. Lithogeochemical Characteristies of the Mesozoic Granitic Intrusion from the Wangxiang Area in Northeastern Hunan Province and Its Tectonic Setting. *Acta Geol. Sin.* **2003**, *77*, 98–103.
46. Xiong, Y.-Q.; Jiang, S.-Y.; Wen, C.-H.; Yu, H.-Y. Granite–pegmatite connection and mineralization age of the giant Renli Ta Nb deposit in South China: Constraints from U–Th–Pb geochronology of coltan, monazite, and zircon. *Lithos* **2020**, *358–359*, 105422. [CrossRef]
47. Changsha General Survey of Natural Resources Center, China Geological Survey. *Proposal for Exploration Block of Yanzhupo Gold Mine in Pingjiang County, Hunan Province*; Changsha General Survey of Natural Resources Center, China Geological Survey: Changsha, China, 2024; pp. 1–62. (In Chinese)
48. Gilbert, S.; Danyushevsky, L.; Goemann, K.; Death, D. Fractionation of sulphur relative to iron during laser abla-tion-ICP-MS analyses of sulfide minerals: Implications for quantification. *J. Anal. At. Spectrom.* **2014**, *29*, 1024–1033. [CrossRef]
49. Liu, Y.; Hu, Z.; Gao, S.; Günther, D.; Xu, J.; Gao, C.; Chen, H. In situ analysis of major and trace elements of anhydrous minerals by LA-ICP-MS without applying an internal standard. *Chem. Geol.* **2008**, *257*, 34–43. [CrossRef]
50. Paton, C.; Hellstrom, J.; Paul, B.; Woodhead, J.; Hergt, J. Iolite: Freeware for the visualisation and processing of mass spectrometric data. *J. Anal. At. Spectrom.* **2011**, *26*, 2508–2518. [CrossRef]
51. Wilson, S.A.; Koenig, A.E.; Ridley, W.I. Development of sulfide calibration standards for the laser ablation inductively-coupled plasma mass spectrometry. *J. Anal. At. Spectrom.* **2002**, *17*, 406–409. [CrossRef]
52. Chu, G.; Chen, H.; Zhang, S.; Zhang, Y.; Cheng, J. Geochemistry and Geochronology of Multi-Generation Garnet: New Insights on the Genesis and Fluid Evolution of Prograde Skarn Formation. *Geosci. Front.* **2023**, *14*, 101495. [CrossRef]
53. Danyushevsky, L.; Robinson, P.; Gilbert, S.; Norman, M.; Large, R.; Mcoldrick, P.; Shelley, M. Routine quantitative multi-element analysis of sulphide minerals by laser ablation ICP-MS: Standard development and consideration of matrix effects. *Geochemistry* **2011**, *11*, 51–60. [CrossRef]

54. Zhang, Y.; Chen, H.; Cheng, J.; Tian, J.; Zhang, L.; Olin, P. Pyrite geochemistry and its implications on Au-Cu skarn metallogeny: An example from the Jiguanzui deposit, Eastern China. *Am. Mineral.* **2022**, *107*, 1910–1925. [CrossRef]
55. Hu, Z.; Zhang, W.; Liu, Y.; Gao, S.; Li, M.; Zong, K.; Chen, H.; Hu, S. Wave Signal-Smoothing and Mercury-Removing Device for Laser Ablation Quadrupole and Multiple Collector ICPMS Analysis: Application to Lead Isotope Analysis. *Anal. Chem.* **2015**, *87*, 1152–1157. [CrossRef] [PubMed]
56. Zhang, W.; Hu, Z.; Gunther, D.; Liu, Y.; Ling, W.; Zong, K.; Chen, H.; Gao, S. Direct lead isotope analysis in Hg-rich sulfides by LA-MC-ICP-MS with a gas exchange device and matrix-matched calibration. *Anal. Chim. Acta* **2016**, *948*, 9–18. [CrossRef]
57. Zhang, W.; Hu, Z.; Liu, Y. Iso-Compass: New freeware software for isotopic data reduction of LA-MC-ICP-MS. *J. Anal. At. Spectrom.* **2020**, *35*, 1087–1096. [CrossRef]
58. Zartman, R.E.; Doe, B.R. Plumbotectonics-the model. *Tectonophysics* **1981**, *75*, 135–162. [CrossRef]
59. Han, R.Y.; Shao, Y.J.; Zhang, Y.; Zhao, L.J.; Wang, X. Ore source and cobalt enrichment mechanism of the Jingchong Cu-Co polymetallic deposit, Northeast Hunan Province. *Geochemistry* **2024**, *unpublished* (In Chinese with English abstract).
60. Li, P. Magmatism of Phanerzoic Granitoids in Southeastern Hunan Province, China and It Evolution Regularity. PhD Thesis, Guangzhou Institute of Geochemistry, Chinese Academy of Sciences, Guangzhou, China, 2006. (In Chinese with English abstract).
61. Liu, H.C.; Zhu, B.Q. Study on the depositional time of the Lengjiaxi Group and Banxi Group in the northwestern Hunan Province. *Chin. Sci. Bull.* **1994**, *39*, 148–150.
62. Large, R.R.; Halpin, J.A.; Danyushevsky, L.V.; Maslennikov, V.V.; Bull, S.W.; Long, J.A.; Gregory, D.D.; Lounejeva, E.; Lyons, T.W.; Sack, P.J.; et al. Trace element content of sedimentary pyrite as a new proxy for deep-time ocean–atmosphere evolution. *Earth Planet. Sci. Lett.* **2014**, *389*, 209–220. [CrossRef]
63. George, L.L.; Biagioni, C.; Lepore, G.O.; Lacalamita, M.; Agrosì, G.; Capitani, G.C.; Bonaccorsi, E.; d'Acapito, F. The specia-tion of thallium in (Tl, Sb, As)-rich pyrite. *Ore Geol. Rev.* **2019**, *107*, 364–380. [CrossRef]
64. Reich, M.; Kesler, S.E.; Utsunomiya, S.; Palenik, C.S.; Chryssoulis, S.L.; Ewing, R.C. Solubility of gold in arsenian pyrite. *Geochim. Et Cosmochim. Acta* **2005**, *69*, 2781–2796. [CrossRef]
65. Deditius, A.P.; Utsunomiya, S.; Renock, D.; Ewing, R.C.; Ramana, C.V.; Becker, U.; Kesler, S.E. A proposed new type of arsenian pyrite: Composition, nanostructure and geological significance. *Geochim. Et Cosmochim. Acta* **2008**, *72*, 2919–2933. [CrossRef]
66. Morishita, Y.; Shimada, N.; Shimada, K. Invisible gold in arsenian pyrite from the high-grade Hishikari gold deposit, Japan: Significance of variation and distribution of Au/As ratios in pyrite. *Ore Geol. Rev.* **2018**, *95*, 79–93. [CrossRef]
67. Kusebauch, C.; Gleeson, S.A.; Oelze, M. Coupled partitioning of Au and As into pyrite controls formation of giant Au deposits. *Sci. Adv.* **2019**, *5*, 5891. [CrossRef] [PubMed]
68. Pokrovski, G.S.; Kokh, M.A.; Proux, O.; Hazemann, J.L.; Bazarkina, E.F.; Testemale, D.; Escoda, C.; Boiron, M.C.; Blanchard, M.; Aigouy, T.; et al. The nature and partitioning of invisible gold in the pyrite-fluid system. *Ore Geol. Rev.* **2019**, *109*, 545–563. [CrossRef]
69. Morishita, Y.; Hammond, N.Q.; Momii, K.; Konagaya, R.; Sano, Y.; Takahata, N.; Ueno, H. Invisible gold in pyrite from epithermal, bandediron-formation-hosted, and sedimentary gold deposits: Evidence of hydrothermal influence. *Minerals* **2019**, *9*, 447. [CrossRef]
70. Chouinard, A.; Paquette, J.; Williams-Jones, A.E. Crystallographic controls on trace-element incorporation in auriferous pyrite from the Pascua epithermal highsulfidation deposit, Chile–Argentina. *Can. Mineral.* **2005**, *43*, 951–963. [CrossRef]
71. Hazarika, P.; Mishra, B.; Chinnasamy, S.S.; Bernhardt, H.-J. Multi-stage growth and invisible gold distribution in pyrite from the Kundarkocha sediment-hosted gold deposit, eastern India. *Ore Geol. Rev.* **2013**, *55*, 134–145. [CrossRef]
72. Deditius, A.P.; Utsunomiya, S.; Ewing, R.C.; Kesler, S.E. Nanoscale "liquid" inclusions of As–Fe–S in arsenian pyrite. *Am. Mineral.* **2009**, *94*, 391–394. [CrossRef]
73. Belousov, I.; Large, R.; Meffre, S.; Danyushevsky, L.; Steadman, J.; Beardsmore, T. Pyrite compositions from VHMS and orogenic Au deposits in the Yilgarn Craton, Western Australia: Implications for gold and copper exploration. *Ore Geol. Rev.* **2016**, *79*, 474–499. [CrossRef]
74. Román, N.; Reich, M.; Leisen, M.; Morata, D.; Barra, F.; Deditius, A.P. Geochemical and micro-textural fingerprints of boil-ing in pyrite. *Geochim. Et Cosmochim. Acta* **2019**, *246*, 60–85. [CrossRef]
75. Liu, Q.-Q.; Shao, Y.-J.; Chen, M.; Algeo, T.J.; Li, H.; Dick, J.M.; Wang, C.; Wang, W.-S.; Li, Z.-Q.; Liu, Z.-F. Insights into the genesis of orogenic gold deposits from the Zhengchong gold field, northeastern Hunan Province, China. *Ore Geol. Rev.* **2019**, *105*, 337–355. [CrossRef]
76. Wang, C.; Shao, Y.; Zhang, X.; Lai, C.; Liu, Z.; Li, H.; Ge, C.; Liu, Q. Metallogenesis of the Hengjiangchong gold deposit in Jiangnan Orogen, South China. *Ore Geol. Rev.* **2020**, *118*, 103350. [CrossRef]
77. Wang, C.; Shao, Y.; Chen, X.; Zhang, X.; Li, H.; Wei, H.; Liu, Q. Genesis of the Jinji gold deposit in the Jiangnan Orogen, South China: Constraints from geology, chlorite geochemistry, age and H-O-S-Pb isotopes. *Ore Geol. Rev.* **2023**, *155*, 105352. [CrossRef]
78. Mao, J.W.; Kerrich, R.; Li, H.; Li, Y. High $^{3}He/^{4}He$ ratios in the Wangu gold deposit, Hunan province, China: Implications for mantle fluids along the Tanlu deep fault zone. *Geochem. J.* **2002**, *36*, 197–208. [CrossRef]

79. Dong, G.J.; Xu, D.R.; Wang, L.; Chen, G.H.; He, Z.L.; Fu, G.G.; Wu, J.; Wang, Z.L. Determination of mineralizing ages on gold ore deposits in the eastern hunan province, South China and isotopic tracking on ore-forming fluids–re-discussing gold ore deposit type. *Geotecton. Et Metallog.* **2008**, *32*, 482–491, (In Chinese with English abstract).
80. Wang, C.; Shao, Y.-J.; Goldfarb, R.; Tan, S.-M.; Sun, J.; Zhou, C.; Zheng, H.; Liu, Q.-Q.; Xiong, Y.-Q. Superimposed Gold Mineralization Events in the Tuanshanbei Orogenic Gold Deposit, Central Jiangnan Orogen, South China. *Econ. Geol.* **2024**, *119*, 113–137. [CrossRef]
81. Zhou, Y.Q.; Dong, G.J.; Xu, D.R.; Deng, T.; Wu, J.; Wang, X.; Gao, L.; Chen, X.G. Scheelite Sm-Nd age of the Huangjindong Au deposit in Hunan and its geological significance. *Geochimica* **2021**, *50*, 381–397, (in Chinese with English abstract).
82. Yuan, Z.K.; Shao, Y.J.; Liu, Q.Q.; Zhang, Y.C.; Wang, Z.L. Genesis of Jiangdong gold deposit in Wangu gold field, Northeast 713 Hunan: Constraints from fluid inclusions and H-O isotope. *Gold Sci. Technol.* **2024**, *32*, 559–578, (in Chinese with 714 English abstract).
83. Zhang, Q.; Pan, J.Y.; Shao, S.X. Lead isotope interpretation of lead sources in some metal deposits in China. *Geochemistry* **2000**, *29*, 231–238, (In Chinese with English abstract).
84. Shen, N.P.; Peng, J.T.; Yuan, S.D.; Zhang, D.L.; Hu, R.Z. Discussion on lead isotopic composition and source of ore-forming materials in Xujiashan antimony deposit, Hubei Province. *Acta Mineral. Sin.* **2008**, *28*, 169–176, (In Chinese with English abstract).
85. Huston, D.L.; Champion, D.C. Applications of lead isotopes to ore geology, metallogenesis and exploration. In *Isotopes in Economic Geology, Metallogenesis and Exploration*; Springer International Publishing: Cham, Germany, 2023; pp. 155–187.
86. Large, R.R.; Danyushevsky, L.; Hollit, C.; Maslennikov, V.; Meffre, S.; Gilbert, S.; Bull, S.; Scott, R.; Emsbo, P.; Thomas, H.; et al. Gold and trace element zonation in pyrite using a laser imaging technique: Implications for the timing of gold in orogenic and carlin-style sediment-hosted deposits. *Econ. Geol.* **2009**, *104*, 635–668. [CrossRef]
87. Gregory, D.D.; Large, R.R.; Halpin, J.A.; Baturina, E.L.; Lyons, T.W.; Wu, S.; Danyushevsky, L.; Sack, P.J.; Chappaz, A.; Maslennikov, V.V. Trace element content of sedimentary pyrite in black shales. *Econ. Geol.* **2015**, *110*, 1389–1410. [CrossRef]
88. Keith, M.; Smith, D.J.; Jenkin, G.R.T.; Holwell, D.A.; Dye, M.D. A review of Te and Se systematics in hydrothermal pyrite from precious metal deposits: Insights into ore-forming processes. *Ore Geol. Rev.* **2018**, *96*, 269–282. [CrossRef]
89. Migdisov, A.A.; Zezin, D.; Williams-Jones, A.E. An experimental study of cobalt (II) complexation in Cl^- and H_2S-bearing hydrothemal solutions. *Geochim. Et Cosmochim. Acta* **2011**, *75*, 4065–4079. [CrossRef]
90. Burisch, M.; Marks, M.A.W.; Nowak, M.; Markl, G. The effect of temperature and cataclastic deformation on the composition of upper crustal fluids—An experimental approach. *Chem. Geol.* **2016**, *433*, 24–35. [CrossRef]
91. Shan, L. Metallogenic System of Copper-Lead-Zinc-Cobalt Polymetallic Deposits Northeastern Hu'nan Province, South China. PhD. Degree Thesis, South China China University of Geosciences, Beijing, China, 2019. (In Chinese with English abstract).
92. Wang, Z.; Li, S.; Xu, D.; Peng, E.; Wang, Y.; Gan, J.; Huang, B.; Zhang, D. Cobalt enrichment mechanism in the Hengdong cobalt deposit, Northeast Hunan Province: Evidence from texture, chemical composition and sulfur isotopic composition of pyrite. *Acta Petrol. Sin.* **2023**, *39*, 2723–2740, (In Chinese with English abstract). [CrossRef]
93. Shan, L.; Wang, C.; Kang, B.; Jiang, J.S.; Wang, L.; Zhang, K.; Li, Y.J. Mineralization Age, Fluid Properties and Metallogenic Model of the Jingchong Co-Cu Deposit in the Central Jiangnan Orogen, South China. *Geotecton. Et Metallog.* **2024**, *48*, 1299–1314, (In Chinese with English abstract).
94. Jia, B.H.; Peng, H.Q. *Precambrian Geology and Mineralization in Northeast Hunan*; Geological Publishing House: Beijing, China, 2005; pp. 106–122. (In Chinese)
95. Bralia, A.; Sabatini, G.; Troja, F. A revaluation of the Co/Ni ratio in pyrite as geochemical tool in ore genesis problems. *Miner. Deposita* **1979**, *14*, 353–374. [CrossRef]
96. Clark, C.; Grguric, B.; Mumm, A.S. Genetic implications of pyrite chemistry from the Paleoproterozoic Olary Domain and overlying Neoproterozoic Adelaidean sequences, northeastern South Australia. *Ore Geology Reviews* **2004**, *25*, 237–257. [CrossRef]
97. Wang, K.; Zhai, D.; Liu, J.; Wu, H. LA-ICP-MS trace element analysis of pyrite from the Dafang gold deposit, South China: Implications for ore genesis. *Ore Geol. Rev.* **2021**, *139*, 104507. [CrossRef]
98. Adam, M.M.A.; Lv, X.; Abdel Rahman, A.A.; Stern, R.J.; Abdalrhman, A.A.A.; Ullah, Z. In-situ sulfur isotope and trace ele-ment compositions of pyrite from the Neoproterozoic Haweit gold deposit, NE Sudan: Implications for the origin and source of the sulfur. *Ore Geol. Rev.* **2020**, *120*, 103405. [CrossRef]
99. del Real, I.; Thompson, J.; Simon, A.C.; Reich, M. Geochemical and Isotopic Signature of Pyrite as a Proxy for Fluid Source and Evolution in the Candelaria-Punta del Cobre Iron Oxide Copper-Gold District, Chile. *Econ. Geol.* **2020**, *115*, 1493–1518. [CrossRef]
100. Liu, W.; McPhail, D.C. Thermodynamic properties of copper chloride complexes and copper transport in magmatic-hydrothermal solutions. *Chem. Geol.* **2005**, *221*, 21–39. [CrossRef]
101. Kouzmanov, K.; Pokrovski, G.S. *Hydrothermal Controls on Metal Distribution in Porphyry Cu (-Mo-Au) Systems In: Geology and Genesis of Major Copper Deposits and Districts of the World: A Tribute to Richard H Sillitoe*; Hedenquist, J.W., Harris, M., Camus, F., Eds.; Society of Economic Geologists: Littleton, CO, USA, 2012; pp. 573–618.

102. Genna, D.; Gaboury, D. 2015. Deciphering the hydrothermal evolution of a VMS system by LA-ICP-MS using trace elements in pyrite: An example from the Bracemac-Mcleod deposits, Abitibi, Canada, and implications for exploration. *Econ. Geol.* **2015**, *110*, 2087–2108. [CrossRef]
103. Keith, M.; Hackel, F.; Haase, K.M.; Schwarz-Schampera, U.; Klemd, R. Trace element systematics of pyrite from submarine hydrothermal vents. *Ore Geol. Rev.* **2016**, *72*, 728–745. [CrossRef]
104. Keith, M.; Smith, D.J.; Doyle, K.; Holwell, D.A.; Jenkin, G.R.T.; Barry, T.L.; Becker, J.; Rampe, J. Pyrite chemistry: A new window into Au-Te ore-forming processes in alkaline epithermal districts, Cripple Creek, Colorado. *Geochim. Et Cosmochim. Acta* **2020**, *274*, 172–191. [CrossRef]
105. Putnis, A. Mineral replacement reactions. *Rev. Mineral. Geochem.* **2009**, *70*, 87–124. [CrossRef]
106. Hu, H.; Lentz, D.; Li, J.-W.; McCarron, T.; Zhao, X.-F.; Hall, D. Reequilibration processes in magnetite from iron skarn deposits. *Econ. Geol.* **2015**, *110*, 1–8. [CrossRef]
107. Hastie, E.C.G.; Schindler, M.; Kontak, D.J.; Lafrance, B. Transport and coarsening of gold nanoparticles in an orogenic deposit by dissolution-reprecipitation and Ostwald ripening. *Commun. Earth Environ.* **2021**, *2*, 57. [CrossRef]
108. Chen, X.-D.; Li, B.; Tang, L.; Zhang, W.-D.; Zhu, L. Silver enrichment and trace element deportment in hydrothermal replacement reactions: Perspective from the Nageng Ag-polymetallic deposit, East Kunlun Orogen, NW China. *Ore Geol. Rev.* **2022**, *142*, 104691. [CrossRef]
109. Ma, Y.; Jiang, S.Y.; Frimmel, H.E.; Zhu, L.-Y. In situ chemical and isotopic analyses and element mapping of multiple-generation pyrite: Evidence of episodic gold mobilization and deposition for the Qiucun epithermal gold deposit in Southeast China. *Am. Mineral.* **2022**, *107*, 1133–1148. [CrossRef]
110. Williams-Jones, A.E.; Heinrich, C.A. Vapor transport or metals and the formation of magmatic-hydrothermal ore deposits. *Econ. Geol.* **2005**, *100*, 1287–1312. [CrossRef]
111. Pokrovski, G.S.; Borisova, A.Y.; Bychkov, A.Y. Speciation and transport of metals and metalloids in geological vapors. *Rev. Mineral. Geochem.* **2013**, *76*, 165–218. [CrossRef]
112. Wohlgemuth-Ueberwasser, C.C.; Viljoen, F.; Petersen, S.; Vorster, C. Distribution and solubility limits of trace elements in hydrothermal black smoker sulfides: An in-situ LA-ICP-MS study. *Geochim. Et Cosmochim. Acta* **2015**, *159*, 16–41. [CrossRef]
113. Velásquez, G.; Beziat, D.; Salvi, S.; Siebenaller, L.; Borisova, A.Y.; Pokrovski, G.S.; De Parseval, P. Formation and deformation of pyrite and implications for gold mineralization in the El Callao District, Venezuela. *Econ. Geol.* **2014**, *109*, 457–486. [CrossRef]
114. Ohmoto, H. Systematics of Sulfur and Carbon Isotopes in Hydrothermal Ore Deposits. *Econ. Geol.* **1972**, *67*, 551–578. [CrossRef]
115. Williams-Jones, A.E.; Bowell, R.J.; Migdisov, A.A. Gold in solution. *Elements* **2009**, *5*, 281–287. [CrossRef]
116. Groves, D.I.; Goldfarb, R.J.; Robert, F.; Hart, C.J.R. Gold deposits in metamorphic belts: Overview of current understanding, outstanding problems, future research, and exploration significance. *Econ. Geol.* **2003**, *98*, 1–29.
117. He, D.Y.; Qiu, K.F.; Simon, A.C.; Pokrovski, G.S.; Yu, H.C.; Connolly, J.A.D.; Li, S.S.; Turner, S.; Wang, Q.F.; Yang, M.F.; et al. Mantle oxidation by sulfur drives the formation of giant gold deposits in subduction zones. *Proc. Natl. Acad. Sci. USA* **2024**, *121*, e2404731121. [CrossRef]
118. Morrison, G.W.; Rose, W.J.; Jaireth, S. Geological and geochemical controls on the silver content (fineness) of gold in gold-silver deposits. *Ore Geol. Rev.* **1991**, *6*, 333–364. [CrossRef]
119. Zhou, X.; Sun, T.; Shen, W.; Shu, L.; Niu, Y. Petrogenesis of Mesozoic granitoids and volcanic rocks in South China: A response to tectonic evolution. *Episodes* **2006**, *29*, 26–33. [CrossRef] [PubMed]
120. Li, Z.-X.; Li, X.-H. Formation of the 1300-km-wide intracontinental orogen and postorogenic magmatic province in Mesozoic South China: A flat-slab subduction model. *Geology* **2007**, *35*, 179–182. [CrossRef]
121. Wen, Z.L.; Deng, T.; Dong, G.J.; Zou, F.H.; Xu, D.R.; Wang, Z.L.; Lin, G.; Chen, G.W. Study on the characters and rules of the ore-controlling structures of the Wangu gold deposit in northeastern Hunan Province. *Geotecton. Et Metallog.* **2016**, *40*, 281–294, (In Chinese with English abstract).
122. Cook, N.J.; Ciobanu, C.L.; Meria, D.; Silcock, D.; Wade, B. Arsenopyrite-pyrite association in an orogenic gold ore: Tracing mineralization history from textures and trace elements. *Econ. Geol.* **2013**, *108*, 1273–1283. [CrossRef]
123. Fougerouse, D.; Micklethwaite, S.; Tomkins, A.G.; Mei, Y.; Kilburn, M.; Guagliardo, P.; Fisher, L.A.; Halfpenny, A.; Gee, M.; Paterson, D.; et al. Gold remobilisation and formation of high grade ore shoots driven by dissolution reprecipitation replacement and Ni substitution into auriferous arsenopyrite. *Geochim. Et Cosmochim. Acta* **2016**, *178*, 143–159. [CrossRef]
124. Rottier, B.; Kouzmanov, K.; Walle, M.; Bendezu, R.; Fontbote, L. Sulfide replacement processes revealed by textural and LA-ICP-MS trace element analyses: Example from the early mineralization stages at Cerro de Pasco, Peru. *Econ. Geol.* **2016**, *111*, 1347–1367. [CrossRef]
125. Sung, Y.-H.; Brugger, J.; Ciobanu, C.L.; Pring, A.; Skinner, W.; Nugus, M. Invisible gold in arsenian pyrite and arsenopyrite from a multistage Archaean gold deposit: Sunrise Dam, Eastern Goldfields Province, Western Australia. *Miner. Depos.* **2009**, *44*, 765–791. [CrossRef]

126. Thomas, H.V.; Large, R.R.; Bull, S.W.; Maslennikov, V.; Berry, R.F.; Fraser, R.; Froud, S.; Moye, R. Pyrite and pyrrhotite textures and composition in sediments, laminated quartz veins, and reefs at bendigo gold mine, Australia: Insights for Ore Genesis. *Econ. Geol.* **2011**, *106*, 1–31. [CrossRef]
127. Fougerouse, D.; Micklethwaite, S.; Ulrich, S.; Miller, J.; Godel, B.; Adams, D.T.; McCuaig, T.C. Evidence for two stages of mineralization in West Africa's largest gold deposit: Obuasi, Ghana. *Econ. Geol.* **2017**, *112*, 3–22. [CrossRef]
128. Wu, Y.F.; Evans, K.; Li, J.W.; Fougerouse, D.; Large, R.R.; Guagliardo, P. Metal remobilization and ore-fluid perturbation during episodic replacement of auriferous pyrite from an epizonal orogenic gold deposit. *Geochim. Et Cosmochim. Acta* **2019**, *245*, 98–117. [CrossRef]